
Numerical modelling of three-dimensional wave-current interactions in complex environment: Application to Alderney Race

Bennis Anne-Claire ^{1,*}, Furgerot Lucille ², Bailly Du Bois Pascal ³, Dumas Franck ⁴, Odaka Tina ⁵, Lathuilière Cyril ⁴, Filipot Jean-Francois ⁶

¹ Normandie Univ., UNICAEN, CNRS, UNIROUEN, Morphodynamique Continentale et Côtière (M2C), Caen, France

² Normandie Univ., UNICAEN, Laboratoire Universitaires des Sciences Appliquées de Cherbourg (LUSAC), Cherbourg en Cotentin, France

³ IRSN, Laboratoire de Radioécologie de Cherbourg (LRC), Cherbourg en Cotentin, France

⁴ Shom, HOM/REC, Brest, France

⁵ University of Brest, CNRS, IRD, Ifremer, Laboratoire d'Océanographie Physique et Spatiale (LOPS), IUEM, Brest, France

⁶ France Energies Marines (FEM), Plouzané, France

* Corresponding author : Anne-Claire Bennis, email address : ac.bennis@unicaen.fr

Abstract :

Modelling three-dimensional wave-current-turbulence interactions in extreme tidal environments is still challenging and necessary for the development of the tidal industry, particularly for the dimensioning of tidal converters. Following this objective, we focus our study on the most energetic tidal site in Western Europe, the Alderney Race (France). Due to the strong tidal current at this location, wave-current interactions were poorly studied by the past and often neglected. We propose to assess how they impact the Alderney Race hydrodynamic by the use of numerical modelling and in-situ measurements. In this study, the following wave-current interactions were observed: (i) Stokes drift effects inducing an increase/decrease in the current depending on the angle between waves and current, with a maximum influence near the surface, (ii) wave enhancement of the bottom friction reducing the tidal current, (iii) refraction of waves by the current, generating changes in waves directions, and (iv) wave breaking ascribed to tidal current, increasing the turbulent mixing. A non-stationary time delay, varying within a same tidal cycle, was noted, which is reduced by including the local wind effects and by adjusting the bottom stress formulation. This study shows that wave-current interactions play a non-negligible role in Alderney Race although the strong tidal current and that they need to consider by the tidal industry.

1. Introduction

Marine renewable energies represent an alternative to fossil energies, which contribute to climate change. Ocean energy from tidal currents has a great potential throughout the world, because the currents are reliable and predictable and could be strong enough for industrial exploitation (e.g. Lynn 2013). In addition, the visual impact of tidal stream devices are limited in comparison to offshore wind farms or some wave energy converters. However, installation and maintenance of tidal converters are more complex than for other technologies due to the particular hydrodynamic conditions of tidal sites. Ocean tidal energy is considered economically feasible for water depths shallower than 50 meters and a flow velocity larger than 2.5 m/s (e.g. Lewis et al. 2015). A key point for the development of tidal energy is resource characterisation, which includes tidal site selection, possible modifications of the hydro-sedimentary environment induced by turbines and the impact of sediment transport on devices.

The most energetic tidal site in Western Europe is the Alderney Race, located in France, between La Hague Cape and Alderney Island, with tidal current reaching 5 m/s during spring tide (e.g. Bahaj and Myers 2004). Field measurements by velocity profilers were conducted in the past to estimate the hydrodynamic resources of the Alderney Race (e.g. Thiebault et al. 2019), but complex conditions generally led to loss or breakage of scientific devices making it very difficult to complete the measurements. Radio-oceanography, with High Frequency (HF) or/and Very High Frequency (VHF) and/or X-band radars, is a relevant option to obtain real-time spatialised measurements of flow velocity and ocean wave characteristics (e.g. Lopez et al. 2019). Numerical modelling is a useful alternative to estimate tidal resources. Because the circulation is primarily driven by astronomical tides, it can be computed with a barotropic model forced by tidal components at its open boundaries (Thiebot et al. 2015). The design of tidal energy converters, however, requires knowledge of the vertical structure of flow velocity in order to assess material fatigue issues and correct assessment of the energy production. Vertical profile depends on tide, as well as on ocean waves, marine turbulence and hydrodynamic interactions. A three-dimensional (3D) fully-coupled wave-current model with an accurate modelling of turbulent mixing is therefore required.

Most of sites that are suitable for tidal converters, including Alderney Race in Normandy (France) and Fromveur in Brittany (France), are influenced by surface waves, that modify the vertical shear of ocean velocity. Major modifications occur near the surface and up to a depth of about one half wavelength, but also near the bottom mainly within the wave and current bottom boundary layers (e.g. Nielsen 1992). Near-surface, ocean velocity may be reduced or accelerated depending on the angle between wave direction and tidal current due to Stokes drift effects (e.g. Kemp and Simons 1983, 1982; Groeneweg and Klopman 1998). Ocean waves also change the vertical shear of the turbulent quantities because of wave-enhancement of

69 turbulence in the bottom boundary layer and near the surface (e.g Grant and Madsen 1979;
70 Burchard 2001). Grant and Madsen (1979) proposed a time-invariant two-layer turbulent
71 model to take into account the wave effects on the turbulence level near and beyond the
72 bottom. Following the same idea, many studies have proposed different formulations for the
73 time-invariant turbulent eddy viscosity (e.g. Christoffersen and Jonsson 1985; Sleath 1991).
74 In the upper ocean, changes in turbulence levels due to waves are mainly caused by wave
75 breaking and Langmuirs circulations (e.g. Agrawal et al. 1992; Craik and Leibovich 1976).

76 Lewis et al. (2017) and Thiebault and Sentchev (2017) explain that the vertical shear
77 of the ocean velocity in tidal areas follows a power law in some cases. However, Lewis
78 et al. (2017) highlight high variability in vertical shear, showing the necessity to improve
79 our understanding of the hydrodynamic processes that cause this variability. Togneri et al.
80 (2017) explain that the well-known turbulent closure $k - \epsilon$ without modifications to include
81 wave effects fails to reproduce the vertical structure of turbulent quantities. They observe
82 an underestimate of turbulent kinetic energy while turbulent dissipation is overestimated.
83 Guillou et al. (2016), Lewis et al. (2014) and Hashemi et al. (2015) have studied the influence
84 of surface waves on the tidal energy estimate. On the whole, they found 10 – 20% variation
85 due to waves, depending on the angle between the tidal current and surface waves. However,
86 these earlier studies are idealised : Guillou et al. (2016) used three-dimensional radiation
87 stresses that are constant over the depth, because they were in shallow waters. In addition,
88 in the latter study, the real case of the Iroise Sea is treated but vertical shear of the ocean flow
89 is not discussed. Lewis et al. (2014) employ the COASWT model (Warner et al. 2010) with
90 three-dimensional radiation stresses of Mellor (2015), which are debated by Arduin et al.
91 (2017) and Mellor (2017), and study an idealised case of a 3D wave-induced flow propagating
92 over a seamount. Hashemi et al. (2015) simulate the real case of the tidal site off the north-
93 western coast of Anglesey Island (Wales, UK), with the inclusion of wave effects, but these
94 simulations are two-dimensional (depth-integrated). Therefore, 3D effects were not taken
95 into account.

96 Ocean waves also influence the bottom friction because they modify the turbulence level
97 near the bottom, particularly inside the wave bottom boundary layer. Grant and Madsen
98 (1979) have conceptualised these processes by a large apparent roughness. Many laboratory
99 and in-situ measurements (e.g Mathisen and Madsen 1996b,a) have supported this concept.
100 Mathisen and Madsen (1999) added the streaming effects to the original form of the apparent
101 roughness model established by Grant and Madsen (1979). Parameterised approaches based
102 on the outputs of these studies have also been developed to formulate the bottom shear
103 stress under waves and current action (e.g. Soulsby et al. 1993; Holmedal et al. 2000) and
104 are widely used by the scientific community when numerical models are not able to explicitly
105 resolve these interactions.

106 We propose to extend the existing studies by performing realistic 3D simulations with a
107 fully-coupled wave-current model (Bennis et al. 2011, 2014, 2016, 2018) in order to unders-
108 tand, how ocean waves and tidal current interact in Alderney Race. The data and methods
109 are described in Section 2 as follows : 2a. Study site and in-situ data, 2b. Numerical mo-
110 delling, 2c. Details on coupling procedure and set-up, and 2d. Description of the numerical
111 experiments. Results are shown and discussed in Section 3 which is divided into four parts :
112 3a. Tidal elevation, 3b. Sea states, 3c. Time series of the tidal stream velocity, and 3d.
113 Vertical structure of the tidal stream velocity. Conclusions are drawn in Section 4.

114 2. Data and Methods

115 a. *Study Site and Data Collection*

116 Alderney Race is located inside the English Channel (hereinafter EC) between the Al-
117 derney Island and La Hague Cape along the French coast, with a depth of 25-65 m (see
118 Figure 1a). Due to the proximity of the Cherbourg harbour and its facilities, that facilitates
119 marine operations, companies are interested in installing of marine currents turbines (MCTs)
120 to produce electricity from tidal current. Alderney Race is a mega-tidal environment (e.g.
121 Dauvin 2015), with a mean spring tidal range varying from 6 to 11 m from the north to the
122 south of La Hague Cape (about 5 km between Anse de Saint Martin : $49^{\circ}42'30''$ N/ $1^{\circ}53'0''$ W
123 and Herqueville : $49^{\circ}40'06''$ N/ $1^{\circ}52'34''$ W) and with a strong tidal asymmetry due to the
124 interactions between tidal flow and bathymetry (see Figure 1b). The particular geometry of
125 the Alderney Race, with the short distance, around 12 kms, between Alderney Island and
126 La Hague Cape, generates a channel effect that accelerates the tidal flow up to 5 m/s during
127 spring tides. The maximum mean potential power is estimated to be 5.1 GW (Coles et al.
128 2017). For comparison, this represents half of the French tidal resource (Bahaj and Myers
129 2004) and is 35% higher than the potential power of Pentland Firth, the best tidal site in
130 United Kingdom.

131 Swells from the Atlantic Ocean propagate through the EC, mainly in the western part
132 because they are often stopped by the Cotentin peninsula. Alderney Race, located west of
133 this peninsula, though protected by the Alderney Island, is influenced by swells (e.g. Lopez
134 et al. 2018). The dominant winds in La Hague Cape are south-west or west, with wind velo-
135 city stronger than 16 m/s about 130 days per year according to the French Weather Service
136 (Météo-France). Thus, Alderney Race sea states are often complex, with superposition of
137 swells and wind-seas. Maisondieu (2016) performed statistical analyses based on the HO-
138 MERE database (Boudiere et al. 2013) for the period between 2003 and 2012. The results
139 were : i) about 40% of sea states had at least 3 swells, ii) about 30% of sea states had at
140 least 2 swells and 1 wind-sea, and iii) about 20% of sea states have at least 1 swell and 1

141 wind-sea. Furthermore, a chaotic sea was observed when the tidal current and wind direc-
142 tions were opposite, with wave heights of about 4 m and wavelengths shorter than 50 metres.
143 Complex sea states also occurred and were recorded during the HYD2M experiments, with
144 significant wave heights of about 8 m. Wave breaking is often observed in Alderney Race
145 due to the interactions between waves and the tidal current, leading to the French name
146 'Raz Blanchard' (In English : 'White Race', named for the frequent white caps in this area).
147 High energy marine turbulent structures are present in Alderney Race because of the very
148 rough nature of the seabed, which leads to the ejection of turbulent cells from the bottom
149 to the surface (Mercier 2019). These structures, a few tens of meters in length, are 3D and
150 visible to the naked eye. They interact with the tidal current and ocean waves. Moreover, the
151 bathymetry is very uneven with features and faults acting as several metre height barriers
152 to the flow (Furgerot et al. 2019). The bottom sedimentology is strongly heterogeneous with
153 sand, pebbles and large rocks (e.g. Larsonneur et al. 1982; Foveau et al. 2017; Furgerot et al.
154 2019).

155 ADCP data were collected by the HYD2M consortium (ADCP) in 2017 (see Figure 1a,
156 yellow cross), using a bottom-mounted 500 kHz Teledyne RDI Sentinel V50. ADCP was
157 located at $49^{\circ}40'50.00''\text{N}/2^{\circ}01'46.44''\text{W}$. The estimated mean depth was about 35 m. The
158 bin size was 1 m and the lowest cell was 2 m above the seabed. ADCP data were collec-
159 ted from 14 October 2017 to 26 February 2018, but only days in the period of 21 to 25
160 November 2017 are considered here. ADCP recorded ocean wave characteristics in addi-
161 tion to measurements of vertical profile of the three components of the flow velocity. All
162 ADCP data were 15 min-averaged. This means that high frequency variations, particularly
163 due to turbulence, were not taken into account in this study, but were presented in Furgerot
164 et al. (2018). Data from Met-Office wave buoys (62103 and 62027), available on EMOD-
165 net platform (<http://www.emodnet.eu>), were also used to validate the wave model, but
166 comparison plots are not shown here. The simulated mean sea level was tested against mea-
167 surements of Shom tidal gauges installed in Cherbourg (TG1, recordings from 1943 to now)
168 and Dièlette (TG2, recordings from 2015 to now). Data are downloadable via the datas-
169 hom portal (<https://data.shom.fr>). Tidal gauge locations are marked in black on Figure 1a.
170 Wind data were collected by Goury Semaphore, that is located 7 km apart ADCP point, at
171 10 meters above ground level.

172 The studied time period is representative of typical conditions in Alderney Race, except
173 for extreme events. The met-oceanic conditions were : i) a tidal range between 4 and 7 m,
174 ii) a tidal current varying from 0.2 m/s to 3 m/s, iii) a significant wave height ranging from
175 0.5 m - 4.5 m (with wind-waves and swells), and iv) a wind speed less than 18 m/s.

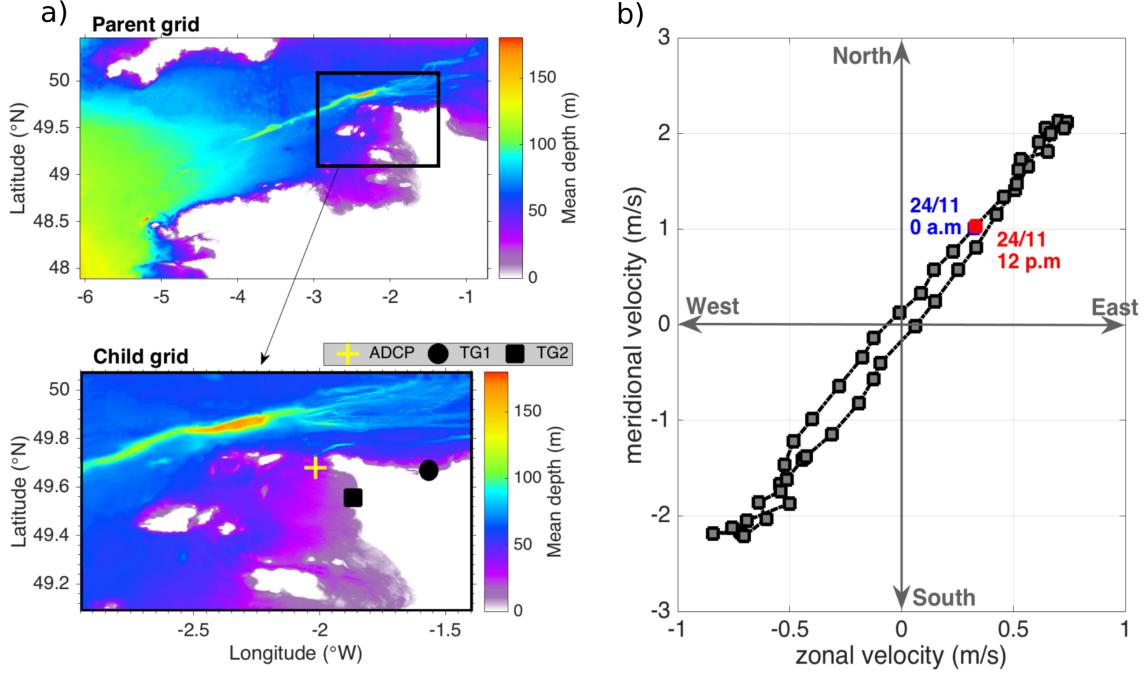


FIGURE 1: (a) ADCP (yellow cross) and tidal gauges (TG1 and TG2 in black circle and square, respectively) over the mean depth (colour scale). (b) Current hodograph for a 12-hour time period on 24 November 2017 between 0 a.m. (blue square) and 12 p.m. (red square).

177 *b. Numerical Modelling Strategy*

178 Our modelling system couples a 3D ocean model, MARS3D v10 (Lazure and Dumas
 179 2008), and the spectral wave model, WAVEWATCH III v4.08 (hereinafter WW3, Tolman
 180 and al. 2014). The wave-driven circulation is computed according to Ardhuin et al. (2008b)
 181 and Bennis et al. (2011). Wave forcing is based on the vortex force method which has been
 182 mainly validated for surf zone and also at coastal scales (e.g. Michaud et al. 2012; Moghimi
 183 et al. 2013; Bennis et al. 2014; Delpey et al. 2014; Bennis et al. 2016). This method consi-
 184 ders the mean flow, represented by the quasi-Eulerian velocity (ie. the Lagrangian velocity
 185 minus the Stokes drift), rather than the total momentum, which removes the tricky problem
 186 of modelling the vertical flux of momentum (Ardhuin et al. 2008a). The generic formula-
 187 tion of momentum equations for a wave-forced, three-dimensional, incompressible, unsteady,
 188 hydrostatic, constant-density flow is :

$$189 \quad \frac{D\hat{\mathbf{U}}}{Dt} = \mathbf{S}_{\text{EPG}} + \mathbf{S}_{\text{VM}} + \mathbf{S}_{\text{HM}} + \mathbf{S}_{\text{WP}} + \mathbf{S}_{\text{BA}} + \mathbf{S}_{\text{BBL}} + \mathbf{S}_{\text{VF}}, \quad (1)$$

190 where $\hat{\mathbf{U}} = (\hat{U}, \hat{V}, \hat{W})$ is the 3D quasi-Eulerian velocity. The source terms \mathbf{S}_{EPG} , \mathbf{S}_{VM} ,

191 \mathbf{S}_{HM} , \mathbf{S}_{BA} , \mathbf{S}_{BBL} , \mathbf{S}_{VF} , \mathbf{S}_{WP} are related to the external pressure gradient, the vertical
192 mixing, the horizontal mixing, the breaking acceleration, the streaming, the vortex force and
193 the wave-induced pressure gradient, respectively. Wave-induced forcing terms are mainly the
194 vortex force, the Bernoulli Head, the forces induced by the wave-to-ocean momentum flux,
195 the wave-induced mixing and the wave-bottom interactions when the wave bottom boundary
196 layer is solved. These terms influence source terms of (1) (more details in Bennis et al. 2011).
197 This set of equations is compatible with that of McWilliams et al. (2004) used in Uchiyama
198 et al. (2010) and Kumar et al. (2012).

199 Horizontal mixing is grid-spacing dependent as in Smagorinsky (1963) with horizontal
200 viscosity (ν_H) defined as $\nu_H = f_{visc} \cdot 0.01 \cdot (\Delta_{xy})^{1.15}$, where Δ_{xy} is the horizontal grid spacing
201 and f_{visc} is a user defined parameter (Okubo 1971).

202 The well-known k- ϵ turbulent scheme, modified according to Walstra et al. (2000) to
203 include ocean wave effects, is used for the vertical mixing :

$$\frac{\partial k}{\partial t} = \frac{1}{D^2} \cdot \frac{\partial}{\partial \zeta} \left(\frac{\nu_V}{s_k} \cdot \frac{\partial k}{\partial \zeta} \right) - \frac{\partial k}{\partial \zeta} \cdot \frac{\partial \zeta}{\partial t} + \text{Prod} + \text{Buoy} - \epsilon + \mathcal{P}_k, \quad (2)$$

$$\frac{\partial \epsilon}{\partial t} = \frac{1}{D^2} \cdot \frac{\partial}{\partial \zeta} \left(\frac{\nu_V}{s_\epsilon} \cdot \frac{\partial \epsilon}{\partial \zeta} \right) - \frac{\partial \epsilon}{\partial \zeta} \cdot \frac{\partial \zeta}{\partial t} + \frac{\epsilon}{k} (c_1 \text{Prod} + c_3 \text{Buoy}) + \mathcal{P}_\epsilon. \quad (3)$$

204 where k is the turbulent kinetic energy and ϵ is the turbulent dissipation. ν_V is the vertical
205 viscosity and depends on both mixing length and turbulent kinetic energy. Coefficients c_1 ,
206 c_3 , s_k and s_ϵ are set according to Warner et al. (2005). Prod and Buoy terms represent the
207 turbulent production by shear and buoyancy, respectively. Equations (2) and (3) differ from
208 the classic ones : two source terms (\mathcal{P}_k and \mathcal{P}_ϵ) were added to include the mixing effects
209 relating to the bottom friction and wave breaking. At the surface, we preferred to use the
210 Dirichlet boundary conditions of Kantha and Clayson (2004), because they are based on
211 friction velocity, rather than the conditions of Walstra et al. (2000). Turbulent source terms
212 depend on wave energy dissipated by bottom friction and wave breaking, near-bottom wave
213 orbital velocity and wave bottom boundary layer thickness. They are linearly distributed
214 over a characteristic depth, that is equal to the root mean square significant wave height
215 divided by two near the surface and to the bottom boundary layer thickness near the bed
216 (more details in Walstra et al. 2000). While other distributions, e.g. trigonometric functions,
217 have been tested, only marginal differences have been noted.

Bottom friction and its enhancement by surface waves is parameterised with the formu-
lation of Soulsby (1995), such that the bottom stress (τ_b) is :

$$\tau_b = |\mathcal{T}_c| \cdot \left[1 + 1.2 \left(\frac{|\mathcal{T}_w|}{|\mathcal{T}_w| + |\mathcal{T}_c|} \right)^{3.2} \right], \quad (4)$$

218 where $|\mathcal{T}_w|$ and $|\mathcal{T}_c|$ are the shear stresses related to waves and current dynamic, such
 219 that :

$$|\mathcal{T}_c| = \rho \left[\frac{\kappa}{\ln\left(\frac{z_m}{z_0}\right)} \right]^2 \cdot |\mathbf{u}_b|^2, \quad (5)$$

220 and

$$|\mathcal{T}_w| = \frac{1}{2} \rho f_w |\mathbf{u}_{orb}|^2. \quad (6)$$

221 where z_0 is the bottom roughness, ρ is water mass density, \mathbf{u}_b and \mathbf{u}_{orb} are the nearbed
 222 ocean velocity and wave orbital velocity, respectively, and κ is Von-Karman's constant (set
 223 to 0.4), f_w is the friction factor defined according to Soulsby (1995) and z_m is a reference
 224 depth above the sea bed (where the flow velocity is assumed to follow a logarithmic law).
 225 Simulations using two different definitions of z_m were carried out and their results were
 226 compared to provide a sensitivity analysis :

227 (H1). z_m is the depth of the grid cell point nearest the bottom,

228 (H2). z_m is a fraction of the mean depth.

229 Wave forcing terms of equations (1), (2), (3) and (4) are calculated using the mean
 230 wave parameters resulting from WW3. It solves the spectral wave action equation in space
 231 and time, from which spectrum based wave parameters, atmosphere-waves and ocean-waves
 232 parameters and many more parameters are derived. The main purpose of this model is to si-
 233 mulate the wave generation by wind, dissipation and redistribution effects, their propagation
 234 by solving :

$$\frac{D\mathbf{N}}{Dt} = \frac{1}{\sigma} (\mathbf{S}_{ln} + \mathbf{S}_{in} + \mathbf{S}_{nl} + \mathbf{S}_{ds} + \mathbf{S}_{bot} + \mathbf{S}_{db} + \mathbf{S}_{tr} + \mathbf{S}_{sc} + \mathbf{S}_{ice} + \mathbf{S}_{ref} + \mathbf{S}_{mud}) \quad (7)$$

235 where $\mathbf{N}(k, \theta; \mathbf{x}, t)$ is the wave action density spectrum which is a function of time (t),
 236 physical space (\mathbf{x}), wave number (k) and wave direction (θ). σ is the intrinsic wave radian
 237 frequency. Source terms are \mathbf{S}_{ln} , \mathbf{S}_{in} , \mathbf{S}_{nl} , \mathbf{S}_{ds} , \mathbf{S}_{bot} , \mathbf{S}_{db} , \mathbf{S}_{tr} , \mathbf{S}_{sc} , \mathbf{S}_{ice} , \mathbf{S}_{ref} , \mathbf{S}_{mud} , respecti-
 238 vely, for the linear wind input, exponential wind input, non-linear wind input, whitecapping
 239 dissipation, dissipation by bottom friction over sandy and rocky beds, depth-induced wave
 240 breaking dissipation, triad wave-wave interactions, bottom scattering, wave-ice interactions,
 241 reflection by shoreline or by floating icebergs and dissipation by viscous mud (more details
 242 can be found in Tolman and al. 2014).

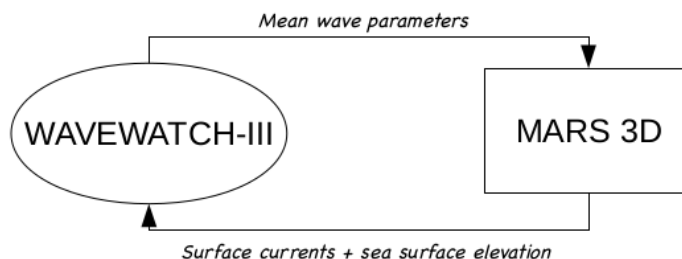
243 For $\mathbf{S}_{in} + \mathbf{S}_{ds}$, formulations of Ardhuin et al. (2010) and Filipot and Ardhuin (2012) (he-
 244 reinafter ST4), and Zieger et al. (2015) (hereinafter ST6) have been tested. They aim to

245 modelise the wind input, the swell dissipation and the wave breaking. Please note that ST4
 246 and ST6 do not use a parametric tail in f^{-5} at high frequencies. For \mathbf{S}_{bot} , two parame-
 247 terisations (hereinafter BT1 and BT4) from the JONSWAP (Hasselmann et al. 1973) and
 248 SHOWEX (Ardhuin et al. 2003) experiments were evaluated. However, the results obtained
 249 with Hasselmann et al. (1973) were not shown here. For \mathbf{S}_{db} , the expression of Battjes and
 250 Janssen (1978) was chosen with the Miche-style shallow water limiter for maximum energy.
 251 For \mathbf{S}_{nl} , the Discrete Interaction Approximation method (Hasselmann et al. 1985) was turned
 252 on. For \mathbf{S}_{ref} , the parameterisation of Ardhuin and Roland (2012) was activated.

253 *c. Coupling Procedure and Numerical Set-up*

254 The two-way coupling procedure was initially built by Bennis et al. (2011, 2013). Now,
 255 exchanges between the two models are managed by the automatic coupler OASIS (Valcke
 256 et al. 2015), instead of PALM (Buis et al. 2008). We defined a coupling time step that
 257 was greater than the models time steps. For each coupling time step, OASIS exchanges
 258 hydrodynamic variables among the two models, which will serve to calculate the forcing
 259 terms, as explained below. MARS computes hydrodynamic fields and sends, through the
 260 OASIS coupler, the surface flow velocities, as recommended by Banihashemi et al. (2017),
 261 and sea surface elevation to WW3. After several integration times, corresponding to one
 262 coupling time step, WW3 sends mean wave parameters, e.g. significant wave height and
 263 Bernouilli head, to MARS. The terms used in Eq. (1), (2), (3), (4), (6) are then calculated
 264 by MARS from these mean wave parameters and the MARS hydrodynamic is re-computed.
 265 Subsequently, the surface sea elevation and surface currents are re-sent to WW3 (see Figure
 266 2), and so on.

267 We define two different coupling modes : i) the one-way mode (hereinafter OW) when
 268 WW3 forces MARS and ii) the two-way mode (hereinafter TW) where the feedback from
 269 MARS to WW3 is included in addition to the forcing of MARS by WW3.



270
 FIGURE 2: Coupling procedure. More details in Bennis et al. (2011).

271 Both models use two nested-grids (hereinafter parent and child grids), with similar
 272 horizontal resolutions (600 m and 120 m), that are shown on Figure 1a. Their South-

273 West and North-East boundaries are : i) for parent grid : 47°53'60.0" N/6°03'32.4" W -
274 50°27'0.0" N/0°43'12.0" W, and ii) for child grid : 49°04'48.0" N/2°56'56.4" W - 50°4'12.0" N/
275 1°23'24.0" W. All MARS simulations are in three dimensions with 12 sigma levels over the
276 vertical. The wave model employs 32 frequencies from 0.04 Hz to 0.7678 Hz and 24 directions
277 leading to a directional step of 15 degrees. Open boundaries of MARS are forced with the
278 Shom CST France atlas that uses 114 tidal components (Leroy and Simon 2003). WW3
279 utilises wave spectra of the HOMERE and Ifremer databases (Boudiere et al. 2013) at its
280 open boundaries. WW3 is forced by NCEP winds from CFSRR re-analysis. The deployment
281 of child grids requires 2D-wave spectra, water levels and flow velocity from their parent grids
282 at boundaries. All runs are coupled, with a one-way/two-way coupling for parent and child
283 grids. The child grid coupling time step is 180 s and 20 s for one-way and two-way runs,
284 respectively.

285 *d. Numerical Experiments*

286 A sensitivity analysis on the influence of main formulations and parameters is necessary to
287 ensure a proper validation. The behaviour of the coupled model is assessed through different
288 parameterisations for wave energy dissipation (ST4, ST6) and bottom friction (BT1, BT4).
289 Moreover, the impact of bottom roughness (z_0) and of the size of the near-bottom logarithmic
290 layer (z_m) are evaluated. Bottom stress in MARS is parameterised according to Eqs. (4), (5),
291 (6) with (H1) and (H2) hypothesis for z_m . Tests are also carried out for the two coupling
292 modes (OW and TW) in order to ensure cross validation. All sensitivity tests are not shown to
293 avoid cluttering. So, only the relevant experiments were presented and they are summarised
294 in Table 1. Runs 3, 4 and 7 included wave effects but not local wind effects while Runs 5 and
295 6 took into account the wave and local wind effects. The wave and wind effects were absent
296 from Run 10 where the hydrodynamic was only driven by tides.

297 Model accuracy is evaluated through the root mean square error (RMSE), normalized
298 root mean square error (NRMSE), BIAS, PBIAS, MAE and R-squared (R^2), which are
299 defined as follows (e.g. Allen et al. 2007b,a) :

$$\text{RMSE} = \frac{1}{N} \sqrt{\Sigma(X_{model} - X_{data})^2}, \quad (8)$$

$$\text{NRMSE} = \frac{\text{RMSE}}{\max(X_{data}) - \min(X_{data})}, \quad (9)$$

$$\text{BIAS} = \frac{\Sigma(X_{model} - X_{data})}{N}, \quad \text{PBIAS} = 100 \times \text{BIAS}, \quad (10)$$

$$\text{MAE} = \frac{\Sigma(|X_{model} - X_{data}|)}{N}, \quad (11)$$

$$R^2 = 1 - \frac{\Sigma(X_{data} - X_{model})^2}{\Sigma(X_{data})^2}, \quad (12)$$

301

302

303 where N is the total number of available samples, X_{model} and X_{data} are related to samples
 304 coming from numerical simulations and in-situ data, respectively. PBIAS gives a measure of
 305 whether the model is systematically underestimating or overestimating the measurements.
 306 The closer the value is to zero the better the model. Performance levels regarding $|PBIAS|$
 307 are categorised as follows ≤ 10 excellent, $10 - 20$ very good, $20 - 40$ good, ≥ 40 poor
 308 (Marechal 2004; Allen et al. 2007a). R^2 is a statistical measure of how close the data to the
 309 fitted regression line. $R^2 = 1$ indicates that model results and data are similar. Performance
 310 levels regarding R^2 are categorised as : ≥ 0.65 excellent, $0.65 - 0.5$ very good, $0.5 - 0.2$ good,
 311 ≤ 0.2 poor (Marechal 2004). The choice of category boundary is subjective, these criteria
 312 are not of the fail/pass type, but valuate the performance in four categories from excellent
 313 to poor.

	Year	Wave energy dissipation	Wave bottom friction	Coupling mode	Local wind effects
Run 3	2017	ST6	BT4	TW	NO
Run 4	2017	ST6	BT4	OW	NO
Run 5	2017	ST4	BT4	OW	YES
Run 6	2017	ST4	BT4	TW	YES
Run 7	2017	ST4	BT4	TW	NO
<i>Run 10</i>	<i>2017</i>	—	—	—	NO

314

TABLE 1: List of numerical experiments according to date, wave energy dissipation formula-
 tion, wave bottom friction parameterisation, coupling mode and the inclusion of local wind
 315 effects. All runs include wave effects except for Run 10 in italics.

316 3. Results and Discussion

317 Model tests against ADCP, wave buoys and tidal gauge data are presented. Numerical
 318 validations are related to tidal elevation, mean wave parameters, wave spectra, time series and

319 vertical profiles of the tidal stream velocity. We investigated how ocean waves interact with
320 the tidal current in Alderney Race for different met-oceanic conditions. Effects of bottom
321 friction, bottom roughness, direction of propagation of wave and current, and turbulence
322 modelling are discussed.

323 *a. Tidal Elevation*

324 Tidal range varies between 4 and 7 m for the studied area and time period. Comparisons
325 between measurements of tidal gauges (TG1 and TG2) and numerical simulations of MARS-
326 WW3 are shown on Figure 3. Our coupled model produces mean sea surface elevation values
327 with a terrestrial definition (IGN 69) for the vertical reference. As TG1 and TG2 measu-
328 rements use the levels of the lowest tide, chart data as vertical references, we shifted the
329 simulated water level with 3.88 m for TG1 and 5.55 m for TG2 as recommended by Shom
330 (2017) to provide a commensurable comparison. This correction, based on the minimum
331 BIAS, is consistent with the measured mean sea level of 3.87 m and 5.45 m in Cherbourg
332 and Dièlette in 2017, respectively (Shom 2017).

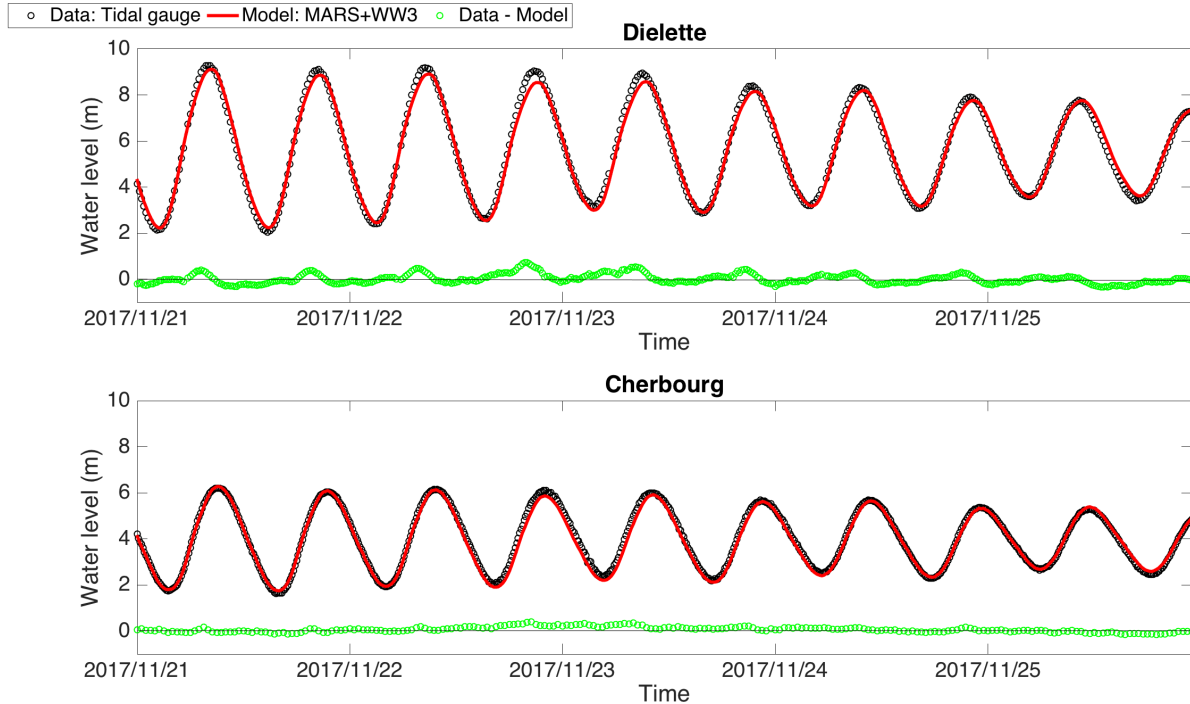
333 Model and data results were close at Cherbourg (TG1), with good fits in amplitude and
334 time phasing (see Figure 3, black dots and red line). Absolute error (hereinafter AE) were
335 around few tens of centimetres, with a maximum values of 0.39 m (see Table 2). RMSE
336 was 0.13 m and $R^2 = 0.98$, that is excellent. Errors mainly occurred just before the high
337 tide, showing that the tidal asymmetry was not well represented in some cases. At Dielette
338 (TG2), numerical simulations were worse than in Cherbourg but they were acceptable, with
339 BIAS = 0.02 m, RMSE = 0.44 m and $R^2 = 0.95$. However, discrepancies were observed with
340 a phase delay up to few minutes for some tidal cycles. In contrast, this problem was absent
341 in Cherbourg (TG1). This illustrates the complexity of the tidal dynamic around La Hague
342 Cape where the tidal range increases by 5 metres within a few kilometres, as shown in Bailly
343 Du Bois et al. (2012). This could be ascribed to bathymetry errors and bottom stress that
344 is strongly impacted by such errors (more details in Section 3c).

		21-25 Nov 2017
TG1 (Cherbourg)	max(AE)	0.39 m
	min(AE)	-0.16 m
	BIAS	0.06 m
	RMSE	0.13 m
TG2 (Dièlette)	max(AE)	0.73 m
	min(AE)	-0.34 m
	BIAS	0.02 m
	RMSE	0.44 m

345

TABLE 2: Maximum (max(AE)) and minimum (min(AE)) values of AE are presented as well as BIAS and RMSE for TG1 and TG2. Positive and negative signs denote under-estimation and over-estimation of water levels by the model, respectively.

346



347

FIGURE 3: Water level at Dielette (TG2, top row) and Cherbourg (TG1, bottom row) measured by Shom tidal gauge (black dots) and computed by the coupled model (red solid line) over 5 days from 21 to 25 November 2017. AE is represented in green dots at each time.

348 *b. Sea States*

349 Sea states in Alderney Race are often complex, with wind seas combined with swells
 350 from the Atlantic Ocean (Maisondieu 2016). Comparisons between numerical simulations and

351 measurements were performed in order to investigate how wave-current interactions influence
352 ocean waves in Alderney Race. Several parameterisations for the wave energy dissipation by
353 whitecapping and bottom friction were evaluated. Moreover, water level and surface current
354 effects on the wave field are presented and discussed as well as local wind effects.

355 Time series of the magnitude (hereinafter U_{10}) and direction (hereinafter $Udir_{10}$) of the
356 wind at 10 metres above ground level (see Figure 4) showed high values for U_{10} during
357 the night of 22-23 November, with a maximum value around 17.5 m/s, and for a North-
358 North-East to South-South-West wind. The wind simulated by CFSRR, that have a spatial
359 resolution of 0.2° of latitude and of 0.1° of longitude at the study site location, is used
360 to force WW3. Wind forcing was in agreement with the wind measured at Goury by the
361 semaphore (see Figure 4). NRMSE is around 0.11 (see Table 3) while PBIAS is positive
362 for U_{10} , indicating that the CFSRR values were higher than the measured ones. However,
363 PBIAS remains very good for U_{10} (around 14%) while MAE is excellent for $Udir_{10}$ (around
364 7%). The discrepandancies can be explained by the coarse resolution of the CFSRR model,
365 the distance (around 7 km) between Goury and the ADCP point (Coelingh et al. 1996, 1998),
366 and also because the semaphore data are recorded above ground level that influences the
367 atmospheric boundary layer and the wind velocity (e.g. Bailly Du Bois and Dumas 2005).
368 The significant wave height recorded by ADCP was highest on 23 November at 2 :13 a.m.
369 and 3 :13 a.m., reaching 4 m and 3.6 m, respectively. During this time period, high winds
370 were measured with U_{10} values greater than 15 m/s. As a result the inclusion of local wind
371 effects has improved the simulated significant wave height (see Figures 5 and 6a, Run 3 vs
372 Run 6, and Table 4), in particular between the 22 November at 12 a.m. and the 23 November
373 at 12 p.m, where U_{10} was highest. NRSME has been reduced by 50% and now reached 0.08
374 for Run 6. PBIAS were high for Run 3 (around 25%) and Run 4 (around 28%) and showed
375 that the significant wave height was largely underestimated by the model. With local wind
376 effects, PBIAS decreased substantially to 5.8% for Run 6 (see Table 4), that is excellent.
377 R-squared values and scatter plots of Figure 5 well illustrated how the local wind effects
378 have improved the fit to data, with $R^2 = 0.97$ for Run 6 instead of 0.87 for Run 3.

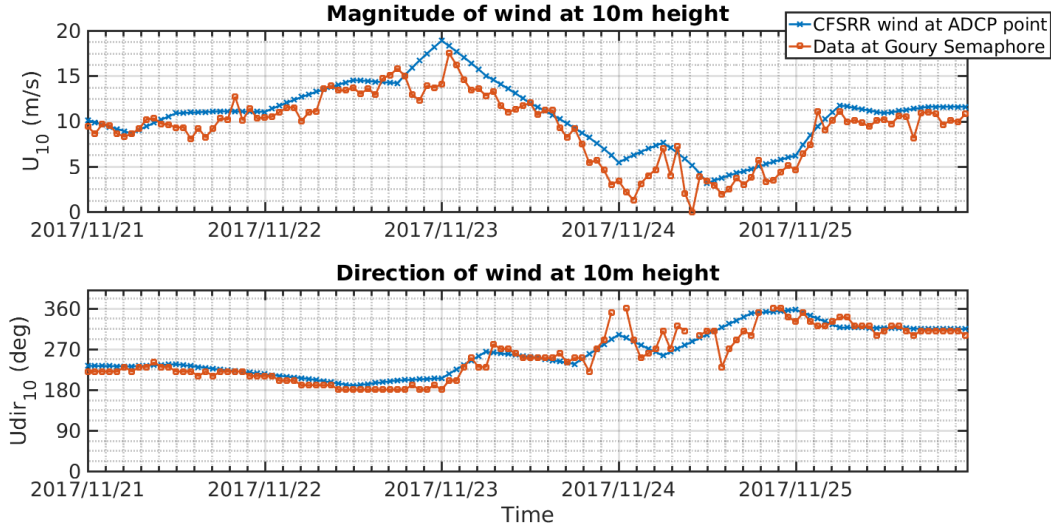
379 The wave-to-ocean momentum flux is enhanced due to local wind effects, particularly for
380 the zonal component, which was 60-fold increase, when wind blows hard (on 23 November
381 around 2 a.m). This increase is ascribed to changes in both wind speed (from 12 m/s on
382 22 November around 12 p.m. to 17.5 m/s on 23 November around 2 a.m) and direction
383 (from South-South-West direction on 22 November around 12 p.m. to West direction on 23
384 November around 2 a.m) during the storm. Wave direction was worse for simulations with
385 local wind effects between the 22 November at 12 a.m. and the 23 November at 12 p.m.
386 compared to the simulations without such effects (see Figure 6b, Run 3 vs Run 6). With
387 local wind effects, waves tend to go towards the North everytime instead of turning East

388 (more explanations hereafter). From the 23 November at 12 p.m to 25 November 11 p.m.,
389 wave direction fitted well to the observations. Therefore, only this time period will study in
390 the next section (3c), which deals with waves effects on tidal currents, because changes in
391 currents due to the waves are partly driven by the direction of propagation of waves, that
392 should be well represented to perform a right analysis.

393 One of most important physical phenomenon in Alderney Race is the wave refraction
394 ascribed to the strong tidal current. This phenomenon was well simulated by the coupled
395 model, particularly when the local wind effects were not included in simulations (see Figure
396 6b, Runs 3 and 6) : refraction has modified wave direction, which was in the agreement with
397 observations and former studies (e.g. Wolf and Prandle 1999; Ardhuin et al. 2012). When
398 wind blowed hard, local wind effects (see Figure 6b, Run 6) tended to smooth refraction
399 effects because currents were abnormally reduced (more details in section 3c) and therefore
400 they had less influence on surface waves. Runs 4 and 5, which did not include neither current
401 effects on waves nor local wind effects, failed to correctly reproduce the measured wave
402 direction. A modulation of significant wave height was also observed due to refraction (Figure
403 6a ; Runs 3 vs 4 or Run 5 vs 6). Both parameterisations for wave breaking dissipation (ST4
404 and ST6) adequately simulated modifications in the significant wave height and wave-to-
405 ocean momentum flux by tide (see Figures 6a,c,d ; Runs 3 vs 4 or Run 5 vs 6). The eastward
406 and northward components of the momentum flux displayed peak values during the ebb,
407 when the tidal current was southwestward (see Figures 6c,d ; Runs 3 vs 6). In that case,
408 interactions between ocean waves and tide generated wave breaking events that produced
409 an enhanced wave-to-ocean momentum flux. This is highly visible if we compare the results
410 of the two coupling modes (see Figure 6c,d ; Runs 3 vs 4 or Run 5 vs 6) : peaks were absent
411 from Runs 4 and 5 because they did not take into account the current effects.

412 Tide also influences the near-bed orbital velocity, and particularly its meridional com-
413 ponent (Figure 6f, Run 3 and 6) because of the tidal current direction, that was NNE/SSW.
414 For the Runs 3 and 6, near-bed orbital velocity was modulated by tides with high and
415 low values during ebb and flood, respectively. In contrast, Runs 4 and 5, being computed
416 without interactions with the flow, did not have such peaks (see Figure 6f), showing the
417 impact of wave-current interactions. The zonal component of the near-orbital velocity was
418 the highest due to the direction of wave propagation, that was mainly from West to East.
419 Its form resembles significant wave height, with maximum values during the night of 22-23
420 November (see Figure 6e). The effects of local wind on the near-bed wave orbital velocity
421 are light in comparison with the tidal ones, except for the 23 November around 2 a.m. where
422 an increase of 5 cm/s was observed due to the strong wind. On the whole, parameterisations
423 for wave bottom friction of Hasselmann et al. (1973) and Ardhuin et al. (2003) produced
424 close near-bed results.

425 The wave-current interactions are also visible on the frequency wave energy spectra (see
426 Figure 8). To study it in details, we selected eight moments that differ in terms of type
427 of wave-current interactions (various waves and current directions, low/high tide, flood/ebb
428 tide, low/high flow velocity). All related informations are summarised in Table 5. All pre-
429 sented spectra were bi-modal with a swell component, where the maximum of energy was
430 located in $f_{p,swell} = 0.07812 H_z$ (RTF2, RTE1 and RTE2) and $f_{p,swell} = 0.09375 H_z$ (RTF1),
431 and a wind-wave component, which reached its maximum in $f_{p,windsea} = 0.125 H_z$ (RTF2,
432 RTE1 and RTE2) and $f_{p,windsea} = 0.1406 H_z$ (RTF1). The splitting frequency (f_c) is around
433 $0.11 H_z$. For the swell component, all runs produced similar results, that are in agreement
434 with the ADCP measurements regardless of coupling mode, wave dissipation parameterisa-
435 tion and local wind effects (see Figure 8). For the wind component, a wave energy decay in
436 f^{-4} for frequencies between $f_{p,windsea}$ and $3f_{p,windsea}$ is observed, as demonstrated by Toba
437 (1973), Donelan et al. (1985) and others. When frequencies were greater than $3f_{p,windsea}$, a
438 decay in f^{-5} is found, as defined in Phillips (1958). Numerical results were consistent with
439 the ADCP data for all runs up to $2f_{p,windsea}$. Runs 5 and 6, which have integrated local wind
440 effects in simulations, overestimated the wave energy beyond $2f_{p,windsea}$ and had an energy
441 tail in f^{-4} . Run 7, which used the same parameterisation for the wave energy dissipation
442 (ST4) than Runs 5 and 6, did not suffer to this overestimation, showing that the influence
443 of local wind effects on ST4.



444 FIGURE 4: Time series for U_{10} (top panel) and $Udir_{10}$ (bottom panel) : CFSRR
inputs are in blue and data from the Goury semaphore are in red.

	NRMSE	R²	PBIAS (%)
U_{10}	0.10	0.96	13.97
$Udir_{10}$	0.11	0.98	3.82

445
446 TABLE 3: NRMSE, R^2 correlation and PBIAS for U_{10} and $Udir_{10}$.

	Runs	NRMSE	R²	PBIAS (%)
447 H_s	Run 3	0.16	0.87	-27.95
	Run 4	0.16	0.87	-25.57
	Run 5	0.10	0.95	12.07
	Run 6	0.08	0.97	5.89

448 TABLE 4: NRMSE, R² correlation and PBIAS for significant wave height (H_s). Runs 3, 4,
5 and 6 are presented.

	Date	W ⊥ C	W+C	U_c^s(m/s)	SSH(m)
449	RTF1 (flood)	23/11/2017 10 :45 p.m.	X		2.01 1.87
	RTF2 (flood)	24/11/2017 00 :45 a.m.	X		1.13 0.67
	RTE1 (ebb)	24/11/2017 02 :45 a.m.		X	0.93 -1.18
	RTE2 (ebb)	24/11/2017 03 :45 a.m.		X	1.99 -1.82
	RTF3 (flood)	25/11/2017 11 :00 a.m.	X		1.87 1.76
	RTF4 (flood)	25/11/2017 01 :45 p.m.		X	0.63 0.11
	RTE3 (ebb)	25/11/2017 04 :15 p.m.		X	1.56 -1.47
	RTE4 (ebb)	25/11/2017 05 :00 p.m.		X	2.07 -1.73

450 TABLE 5: Waves-current direction (W ⊥ C when waves and current direction are orthogonal and W + C for an angle between waves and current direction less than 80°), surface current velocity (U_c^s) and sea surface height (SSH) at RTF1, RTF2, RTE1, RTE2, RTF3, RTF4, RTE3 and RTE4. Directions follow the oceanographical convention for the flow and the meteorological convention for waves. Values are from numerical simulations.

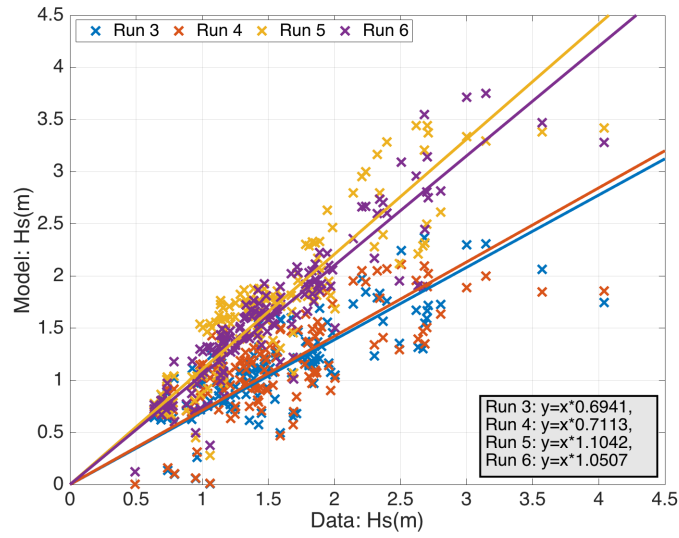
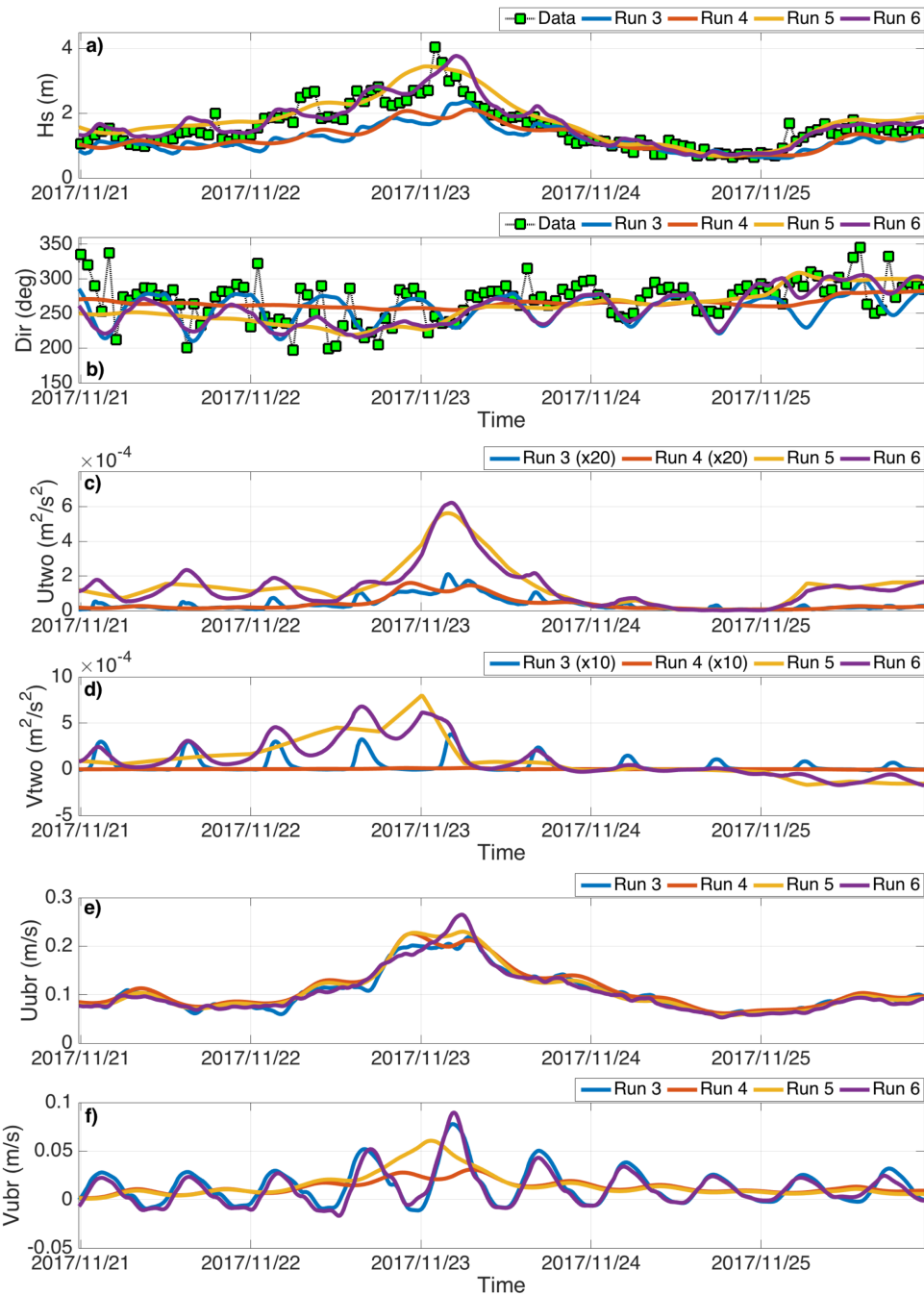


FIGURE 5: Scatter plots for the significant wave height (H_s) for Run 3 (blue crosses), Run 4 (red crosses), Run 5 (yellow crosses) and Run 6 (purple crosses). In-situ data and model results are drawn along x-axis and y-axis, respectively. Regression lines are plotted in blue, red, yellow and purple solid lines for runs 3, 4, 5 and 6, respectively.



452

FIGURE 6: Time series of sea states characteristics, from 21 to 25 November 2017, integrated over frequencies (32) and directions (24) : a) significant wave height, b) wave direction (meteorological convention), c) zonal component of wave-to-ocean momentum flux, d) meridional component of wave-to-ocean momentum flux, e) zonal component of near-bed wave orbital velocity, f) meridional component of near-bed wave orbital velocity. ADCP data are in black-green squares while numerical results for Runs 3, 4, 5 and 6 are in blue, red, yellow and purple solid lines, respectively.

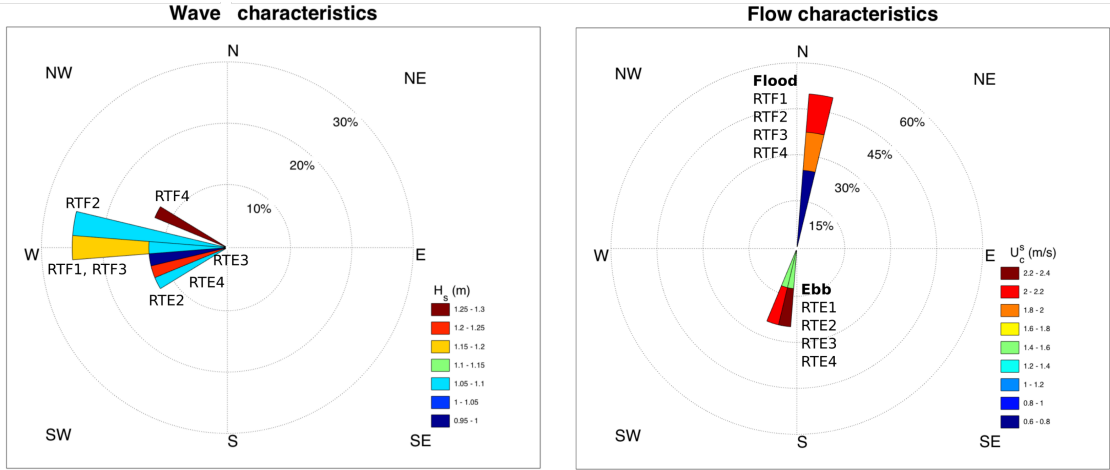


FIGURE 7: Left panel : Wave direction (polygon) and significant wave height (color). Right panel : Direction (polygon) and velocity magnitude (color) of the current. Only RTF1, RTF2, RTE1, RTE2, RTF3, RTF4, RTE3 and RTE4 are shown. Directions follow the oceanographical convention for the flow and the meteorological one for waves. Results are from numerical simulations.

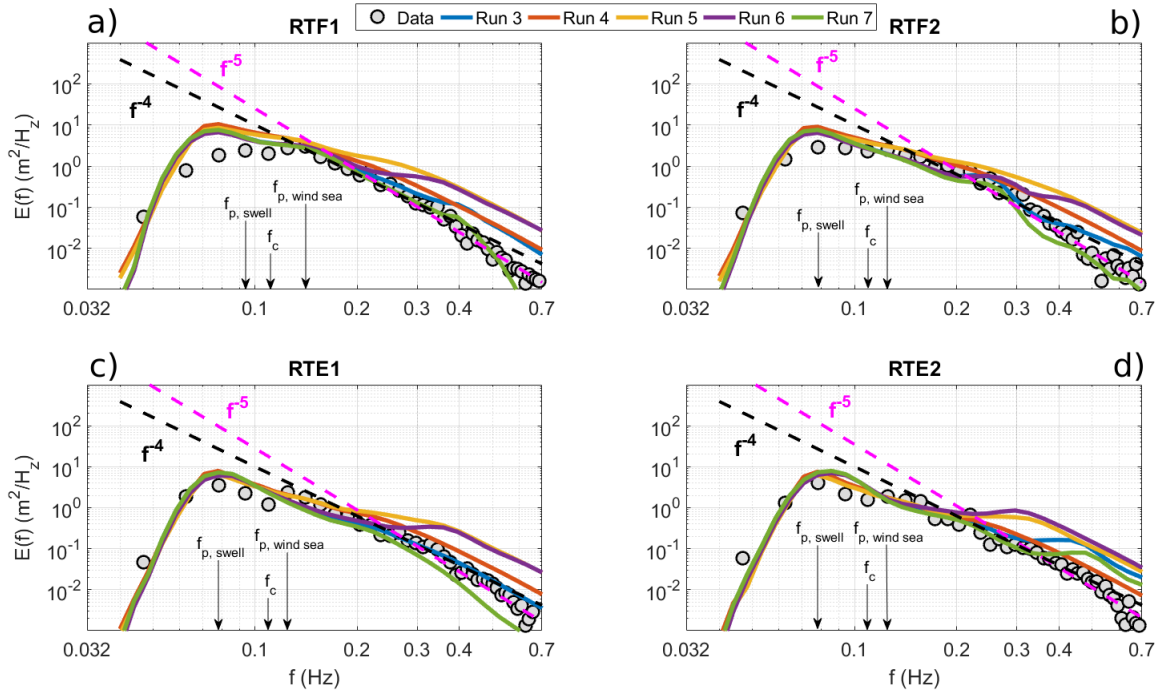


FIGURE 8: Frequency wave energy spectra at : a) RTF1, b) RTF2, c) RTE1 and d) RTE2. The first (a,b) and second (c,d) rows are for flood and ebb tides, respectively. Magenta and black dashed lines are for $o(f^{-5})$ and $o(f^{-4})$, respectively. Note that the x-axis and y-axis are a log10 scale. $f_{p,swell}$, $f_{p,windsea}$, f_c (around $0.11 H_z$) represent the peak frequency for swell and wind sea, and the splitting frequency, respectively.

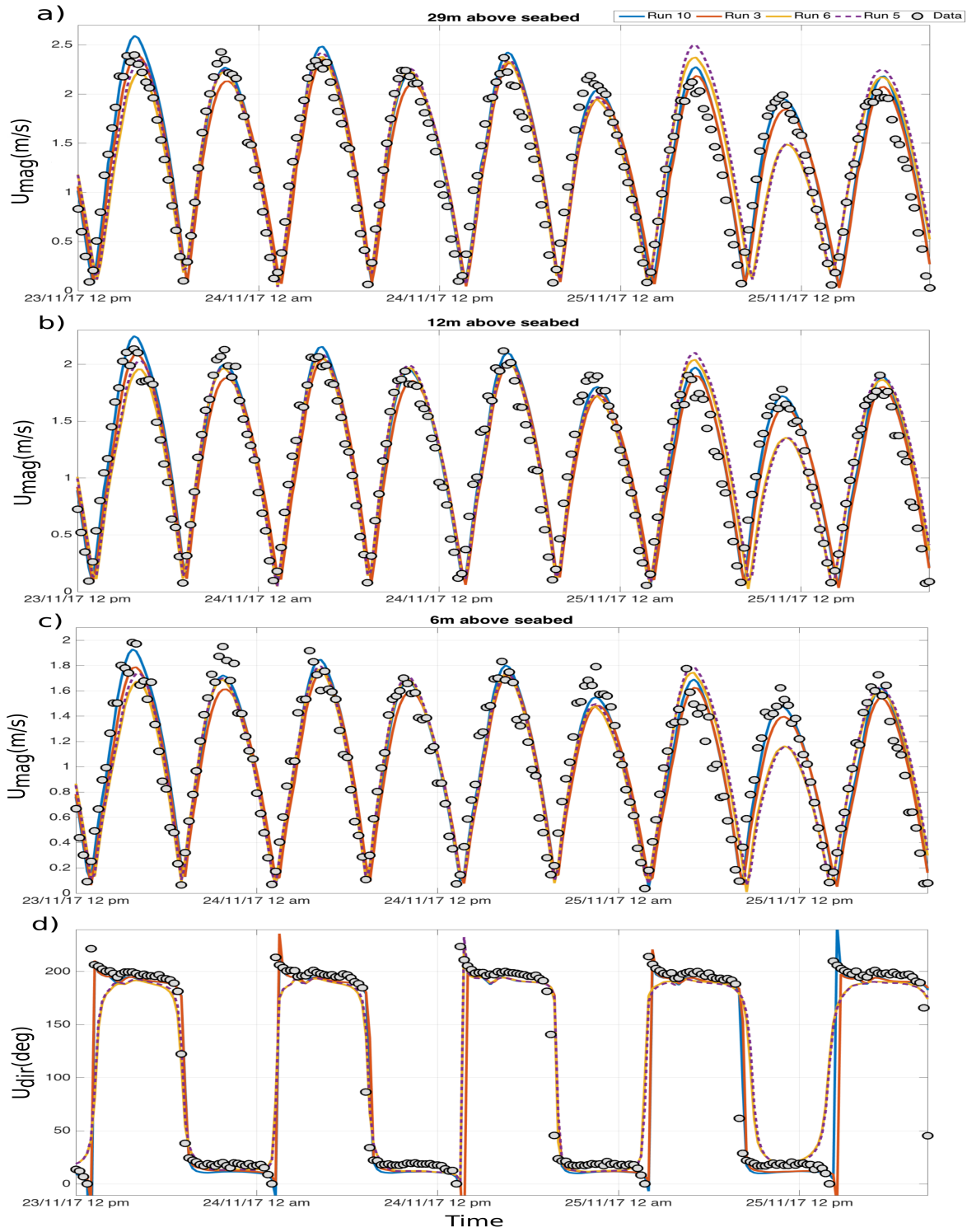
455 *c. Time Series of the Tidal Stream Velocity*

456 We now investigate how the Alderney Race circulation was impacted by ocean waves.
457 Figure 9 shows time series of magnitude and direction of the measured current velocity at 25,
458 12 and 6 meters depth above seabed at the ADCP location between 23 November 2017 at 12
459 p.m and 25 November 2017 at 8 p.m, where the tidal flow velocity varied between 0 and 2.5
460 m/s. First, we start by discussing the results without local wind effects (Runs 3 and 10). On
461 the whole, the numerical results for cases with (Run 3) and without waves (Run 10) were
462 consistent with the data and were close each other (see Figures 9 and 10 and Table 6). Good
463 and similar NRSME (0.09 and 0.11) and R^2 (0.97 and 0.98) for both runs were observed.
464 PBIAS were excellent, because they range from 0.6% to 3.8%, but they showed that velocity
465 was underestimated by the model when wave effects were activated while an overestimate
466 occurred where wave effects were disabled. Wave effects tend to reduce systematically the
467 velocity magnitude (e.g. Grant and Madsen 1979; Xie et al. 2001; Zhang et al. 2004) due to
468 wave enhancement of bottom friction. At low tide, as the model without waves overestimated
469 tidal velocity, simulations with waves had a better fit with in-situ data. Flow direction (see
470 Figure 9d), and its changes belonging to the tidal cycle were well reproduced by the model.
471 Close results were obtained for Run 3 (TW mode) and Run 4 (OW mode, not displayed
472 here). Even if current and sea level produced significant changes in the wave field (see Figure
473 6), the impact of feedback on the tidal current and water level remained weak.

474 As regards the cases taking into account local wind effects (Runs 5 and 6) and between the
475 23 November 12 p.m. and 25 November 2 a.m., tidal current were little impacted by local wind
476 effects and numerical results were close to the data (see Figure 9). Indeed, NRMSE (around
477 0.11), R^2 (around 0.97) and PBIAS (0.62% – 3.79%) were in the same order of magnitude
478 for Run 3 (without local wind) and Run 6 (with local wind). That could be explained by
479 the wind speed at the ADCP point which was weak for this time period, ranging from 4 to
480 10 m/s (see Figure 4). Beyond the 25 November at 2 a.m., when the wind started blowing,
481 a strange behaviour was observed, particularly during the flood with a change in current
482 direction, that induced a loss in the current intensity of around 0.5 m/s, with a smoother
483 transition between ebb and flood directions and a shift in direction to the East. As the tidal
484 current direction was modified, wave-current interactions were impacted. The decrease in
485 velocity magnitude being similar for Runs 5 and 6, that is not induced by a change in wave
486 field due to wave-current interactions. During this time period, waves went towards the East
487 (see Figure 6b), and therefore the change in tidal current direction has reduced the angle
488 between waves and current, leading to a decrease in the current intensity, as reported by
489 Groeneweg and Klopman (1998). As a result, this problem comes from the ocean model
490 MARS and suggests a mis-evaluation of the wind effects on the flow and particularly of the
491 wind stress. Further investigations are required.

492 We noted an occasional phase delay that varied over time from 0 to 30 min. The delays
493 differed depending to the tidal cycles. For example, in tidal cycles containing RTF1, RTF2,
494 RTE1 and RTE2, the phase delay was constant at 15 min and in the same direction for all
495 runs, regardless the coupling mode and the local wind effects. In contrast, we noted different
496 time delays at RTF3 (no time delay for runs with and without local wind effects), RTF4
497 (30 min and no time delay for runs without and with local wind effects, respectively), RTE3
498 (30 min and no time delay for runs without and with local wind effects, respectively) and
499 RTE4 (15 min for runs with and without local wind effects) times, which were part of the
500 same tidal cycle. It is interesting to see that the delay was removed in simulations with local
501 wind effects at RTF3, RTF4 and RTE3. That suggests that time delay could be due to waves
502 and wind through the bottom stress, which was based on the near-bed wave orbital velocity.
503 In addition, the maximum value of 30 min often corresponded to the reverse tide occurring
504 sooner in the in-situ dataset. At this time, waves effects on the current were strongest. To
505 investigate the role of waves and wind, measurements of the near-bed wave orbital velocity
506 are required.

507 Furthermore, time delay could be partially corrected by expressing z_m (Eq. (5)) as a
508 fraction of the mean depth (D). In this study and after many simulations, the fraction was
509 set to 5%. Some sensitivity tests were performed with z_m at 50% (Uchiyama et al. 2009),
510 26.7%, 11.4%, 5.71%, 2.67% and 1.33% of D and the related velocities are presented in
511 Figure 11. A one-hour delay was observed, as shown on Figure 11, between both extreme
512 cases (50% and 1.33% of D), highlighting the link between the bottom stress formulation
513 and time delay. Tidal asymmetry also appeared also to be sensitive to the z_m value, with
514 differences between tidal phases that were accentuated by large z_m values. Because the
515 depth where the logarithmic profile is imposed was strongly dependent on the turbulence
516 level, these tests showed that one of the sources of the time delay was ascribed to the
517 modification of the turbulence level by the interactions between seabed morphology, ocean
518 waves and tidal current. Parameterisation using an apparent roughness as recommended by
519 Grant and Madsen (1979); Signell et al. (1990); Mathisen and Madsen (1999) may be a way
520 of improvement, in addition to use of high spatial resolution bathymetry based on Furgerot
521 et al. (2019).



522

FIGURE 9: Time series of magnitude (a,b,c) and direction (d) of the current velocity at 29 m (a), 12 m (b,d), 6 m (c) depth above seabed. All panels show numerical results for Runs 3 (TW, red solid line), 5 (OW+local wind effects, purple dash line), 6 (TW+local wind effects, yellow solid line) and 10 (without waves, blue solid line). In-situ data are shown with black circles. Directions are based on oceanographic conventions.

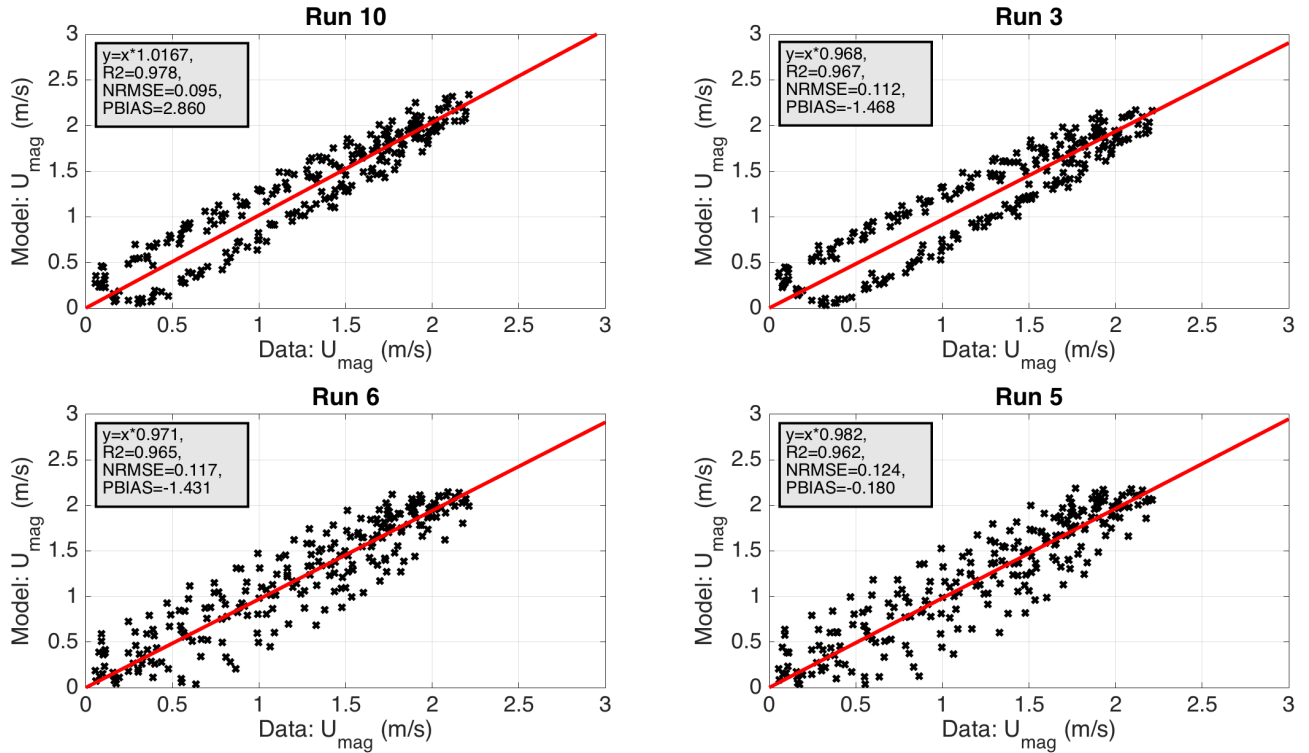
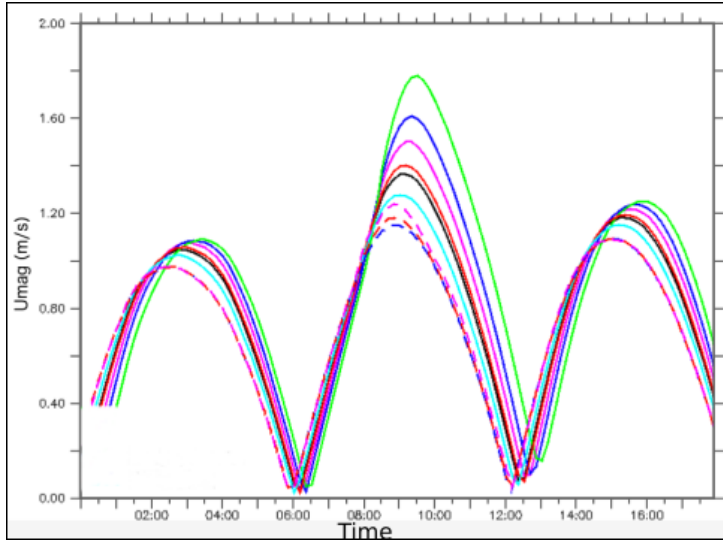


FIGURE 10: Scatter plots for the velocity magnitude (black crosses) at 15 metres above seabed for Run 10, Run 3, Run 6 and Run 5. In-situ data and model results are drawn along x-axis and y-axis, respectively.

	Runs	NRMSE	R ²	PBIAS (%)
z = 29 m	Run 3	0.11	0.97	-0.62
	Run 5	0.14	0.95	1.92
	Run 6	0.12	0.96	-0.41
	Run 10	0.10	0.98	3.76
z = 12 m	Run 3	0.11	0.97	-1.78
	Run 5	0.12	0.96	-0.44
	Run 6	0.11	0.97	-1.66
	Run 10	0.09	0.98	2.58
z = 6 m	Run 3	0.10	0.97	-3.79
	Run 5	0.11	0.96	-2.33
	Run 6	0.11	0.96	-3.53
	Run 10	0.09	0.98	0.74

TABLE 6: NRMSE, R² correlation and PBIAS for velocity magnitude at different depths (29m, 12m and 6m). Runs 3, 5, 6 and 10 are presented.



526

FIGURE 11: Time series of the velocity magnitude for different values and formulations of z_m parameter. Simulations do not include wave effects and used a z_0 equal to $0.008 m$. Reference test was based on the quadratic formulation (black solid line). Green line is for Uchiyama et al. (2009) using $z_m = 50\%D$. Other lines represent current velocity simulated with z_m set to $26.7\%D$, $11.4\%D$, $5.71\%D$ and $2.67\%D$ for the solid blue, magenta, red, cyan lines. Dashed blue, red and magenta lines are for $z_m = 1.33\%D$ and using Okubo (1971) with $f_{visc} = 17$, $f_{visc} = 10$ and Smagorinsky (1963), respectively.

527

528 *d. Vertical Structure of the Tidal Stream Velocity*

529 The vertical shape of the tidal stream velocity in Alderney Race is known to depend
 530 primarily on the tidal phase, surface wave effects, bottom friction and turbulent mixing.
 531 Thibault and Sentchev (2017) and others (e.g. Lewis et al., 2017) found that, in some parti-
 532 cular cases, the vertical shear of the tidal sea current follows a power law (see Eq. (1) of Lewis
 533 et al., 2017) scaled with a roughness coefficient. This form fits well with their data for a calm
 534 sea. Otherwise, they showed that ocean waves, when their effects are significant, change the
 535 shear flow and increase the error between model and measurements. They recommend the
 536 use of a 3D fully wave-current model, which is what we used here. It is not easy to compare
 537 vertical profiles of the flow to observations in a location such as Alderney Race. Indeed, there
 538 are some difficult issues : i) the very rough bottom ejects intermittent 3D highly energetic
 539 turbulent eddies that modify the vertical shape of the flow, ii) the phase delay complicates
 540 the comparison : all presented plots are corrected by phase delay by adjusting the tide rever-
 541 sal time, iii) measurements near the surface lack precision because they have been filtered
 542 to eliminate spurious values induced by the acoustic signal reflection on the sea surface, but

543 also by the air bubbles from wave breaking turbulence, and iv) ocean waves and current are
 544 orthogonal most of the time, which brings us further away from simple case where ocean
 545 waves and current directions are aligned or opposite. We need to define a scale to perform
 546 the analysis : waves and current are considered as opposite for $|\Delta\theta_{w/c}| = 180^\circ$, aligned for
 547 $|\Delta\theta_{w/c}| = 0^\circ$ and orthogonal for $|\Delta\theta_{w/c}| = 90^\circ$, with $|\Delta\theta_{w/c}|$ the angle between waves and
 548 tidal current directions of propagation. Despite these issues, we compared vertical profiles
 549 to in-situ measurements.

550 Comparisons between model and data results were carried out at RTF1, RTF2, RTE1,
 551 RTE2, RTF3, RTF4, RTE3 and RTE4, where tidal current and wave directions differed as
 552 well as tide conditions (see Table 5). Some statistical calculations were performed for the
 553 velocity magnitude. NRSME varied from 0.02 to 0.15, except at RTF3 where a value of
 554 0.36 was reached in case of Run 6. R-squared ranged from 0.96 to 0.99 except at RTF3
 555 for Run 6 where it was around 0.92. PBIAS showed that sometimes model overestimated
 556 the measured velocity and sometimes underestimations occurred. PBIAS were less than
 557 4%, which is excellent, except for Run 6 at RTF2 and RTF3 where they were around 21%.
 558 Therefore, statistical parameters showed a very good agreement ($R^2 \geq 0.96$, $\text{NRMSE} \leq 0.15$,
 559 $\text{PBIAS} \leq 4\%$) between in-situ measurements and model results for all runs, except for Run
 560 6 at RTF3 and RTF2. Discrepancies for Run 6 are due to the mis-evaluation of local wind
 561 effects in the ocean model when wind blowed hard, as explained before. However, these
 562 parameters do not allow us to analyse if the vertical shapes were along the right direction.

563 For flood cases, at RTF1, RTF2, RTF3, wave and current directions were orthogonal
 564 while at RTF4 $|\Delta\theta_{w/c}|$ was around 80° . At RTF4, simulations with wave effects (Runs 3
 565 and 6) produced higher velocity than the one without wave effects (Run 10). The wave
 566 forcing had improved the results, that were consistent with the ADCP data. Runs 6 and 3
 567 velocities were different by their vertical structure : from 20 to 30m depth above seabed, Run
 568 6 velocity was reduced while, for Run 3, the velocity was increased. Both vertical structures
 569 being in agreement with the measurements, it is difficult to conclude. However, these forms
 570 in the upper part of the water column represent different type of wave-current interactions :
 571 aligned waves and current cause a decrease in surface flow while opposite waves and current
 572 accelerate the surface flow due to Stokes drift effects (e.g. Groeneweg and Klopman 1998).
 573 As explained previously, at RTF4, when local wind effects were included in the simulations
 574 (Run 6), the angle between waves and current tended to become small, and as a result the
 575 surface flow velocity was decreased. That what we are seen in Figure 12.

576 At RTF2, inappropriate boosting of the flow was visible when the wave forcing is acti-
 577 vated, while Run 10 (without waves) fitted well to the data. The inclusion of the local wind
 578 effects in simulations had worsened the results. However, the form of the vertical profiles
 579 with wave effects (Runs 3 and 6) was good in comparison to measurements except for near

580 the seabed, showing that the discrepancies came from the bottom friction, which appeared
 581 as being mis-evaluated.

582 For RTF1 and RTF3, the results with and without waves (Runs 3, 6 10; see Figure 12)
 583 were quite similar and fitted the ADCP data. Wave effects had little improved the results by
 584 reducing the velocity, except for Run 6 at RFT3. At these time points, as the tidal current
 585 was higher at about 1.9 m/s at the surface (see Table 5) and the waves were small (see Figure
 586 6a), the wave effects were overwhelmed by the tidal effects and particularly those ascribed
 587 to Stokes drift, which were in the order a few cm/s. At RTF3, as explained previously, the
 588 tidal current was abnormally reduced.

589 During the ebb, at RTE1, RTE2, RTE3 and RTE4, $|\Delta\theta_{w/c}|$ were less than 90° and around
 590 60° . For all time points, waves effects had improved the results by reducing the velocity in
 591 the upper water column due Stokes drift effects, as expected in the former studies. Nice
 592 fits with observations were obtained, particularly at RTE3 and RTE4 where waves are more
 593 energetic than at RTE1 and RTE2 (see Figure 6). Local wind effects, which had induced
 594 error during the flood on 25 November, had not worsened the vertical structure at RTE3
 595 and RTE4.

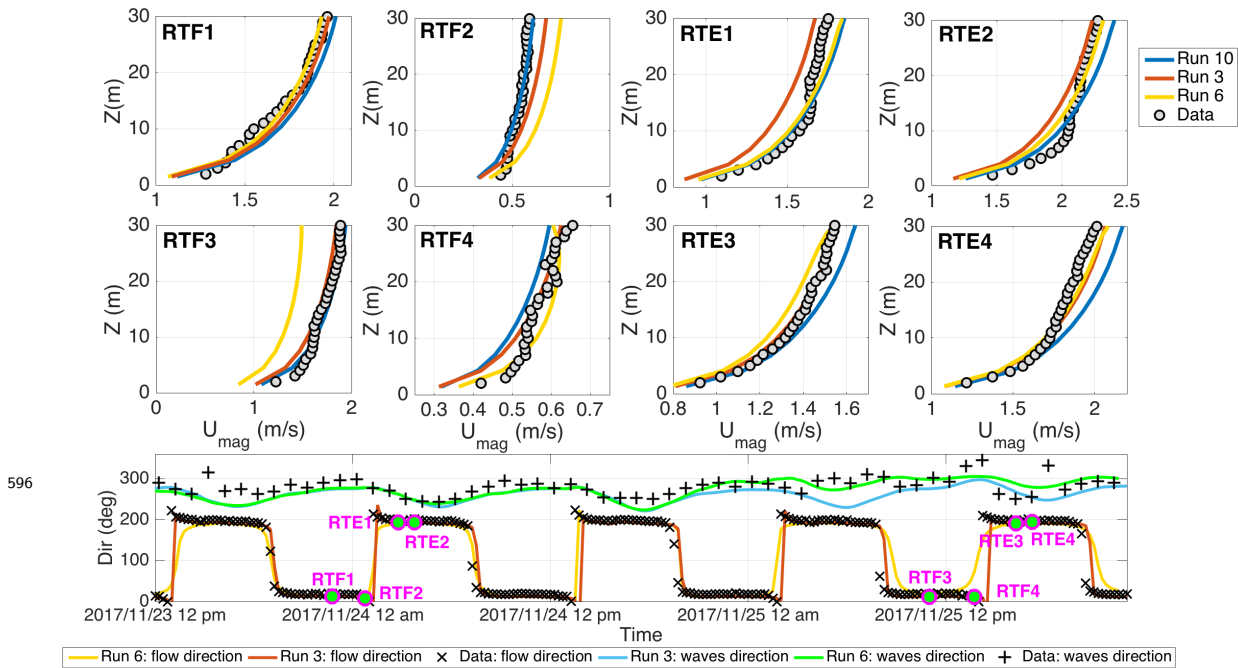


FIGURE 12: **Top and middle panels** : Flow velocity magnitude over depth at RTF1, RTF2, RTE1, RTE2, RTF3, RTF4, RTE3 and RTE4; in-situ measurements are in black circles while numerical results for Runs 3, 6 and 10 are in red, yellow and blue lines, respectively. **Bottom panel** : Time series of the flow direction for Run 3 (red line) and 6 (yellow line) and the related wave direction in light blue and green line, respectively. Measured wave and current directions are in black crosses and plusses.

4. Conclusions and perspectives

The purpose of this study is twofold with a first step dealing with the validating of our modelling platform for the study site and a second step aiming to show the impacts of wave-current interactions on the hydrodynamic of the Alderney Race. To reach these goals, realistic 3D fully-coupled wave-current-turbulence simulations have been carried out and tested against in-situ measurements.

On the whole, our numerical model is successfully validated through statistical parameters (PBIAS, NRMSE, MAE, R^2) in comparison with observations for mean sea water level, significant wave height, mean wave direction, frequency wave energy spectra, flow velocity magnitude and direction. However, a non-stationary time lag was observed sometimes between model and measurements. This problem was found to be sensitive to the waves and wind effects and had been partially fixed when these effects were included, probably due to the near-bed wave orbital velocity which changes the bottom stress. In addition, time lag was also shown as being modified by the depth where a logarithmic velocity profile is applied, highlighting the effects of the near-bed turbulence. Therefore, further studies are required to investigate what are the role in the time lag of the bottom turbulence, near-bed wave orbital velocity as well as the bathymetry effects, that drive the hydrodynamic. Furthermore, when the wind blowed hard (wind speed greater than 15 m/s), the flow velocity was abnormally decreased (of about 0.5 m/s) due to a mis-evaluating of the local wind effects in the ocean model. This point needs to be improved in the future by working on the wind stress formulation and the relating wave contribution.

Wave-current interactions were observed in Alderney Race. Ocean waves impacted the flow due to : - the Stokes drift effects, that induced an increase/decrease in the current depending on the angle between waves and current, with a maximum influence near the surface, - the wave enhancement of the bottom friction that reduced the tidal current. Furthermore, tidal current has modified ocean waves through : - the refraction of waves by the current, that have generated changes in waves directions and - the wave breaking ascribed to tidal current, that increased the turbulent mixing within the water column. The main results of this paper is the significant influence of ocean waves on the vertical profile of the flow whereas waves are small (significant wave height less than 1.5 m). Moreover, changes in vertical profiles were occurred even for a strong surface current (around 2.3 m/s) due to the angle between waves and flow direction.

Consideration of ocean waves effects has improved the simulation of the tidal current and particularly the reproduction of its vertical shape, showing that these effects have to be taken into account for the tidal converter dimensionning.

Acknowledgments

Authors are supported by the HYD2M project (ANR-10-IEED-0006-07) funded by the program called "Investissements d'avenir" for the building of France Energies Marines. Authors acknowledge L. Coquart, V. Garnier, M. Accensi and A. Thévenin for their technical helps. Authors are grateful to F. Ardhuin for providing the WAVEWATCH-III forcing fields. Authors thank Shom to make available their ADCP data in the framework of HYD2M. Results acquired with the Ifremer MARS software. The authors acknowledge the Pôle de Calcul et de Données Marines (PCDM) for providing CAPARMOR and DATARMOR (storage, computational resources, visualization, support services). Simulations have also benefited of the computing facilities of CRIANN. A.-C. Bennis warmly thanks P. Bousquet-Melou for his technical help during the migration step of the coupled model from CAPARMOR to CRIANN. Authors acknowledge the two anonymous reviewers for their useful comments.

Références

- Agrawal, Y. C., E. A. Terray, M. A. Donelan, P. A. Hwang, A. J. Williams, W. Drennan, K. Kahma, and S. Kitaigorodskii, 1992 : Enhanced dissipation of kinetic energy beneath breaking waves. *Nature*, **359**, 219–220.
- Allen, J. I., J. T. Hold, J. Blackford, and R. Proctor, 2007a : Error quantification of a high-resolution coupled hydrodynamic-ecosystem coastal-ocean model : Part 2. Chlorophyll-a, nutrients and SPM. *J. Mar. Sys.*, **68**, 381–401.
- Allen, J. I., P. J. Sommerfield, and F. J. Guilbert, 2007b : Quantifying uncertainty in high-resolution coupled hydrodynamic-ecosystem models. *J. Mar. Sys.*, **64**, 3–14.
- Ardhuin, F., A. D. Jenkins, and K. Belibassakis, 2008a : Commentary on ‘the three-dimensional current and surface wave equations’ by George Mellor. *J. Phys. Oceanogr.*, **38**, 1340–1349.
- Ardhuin, F., W. C. O’Reilly, T. H. C. Herbers, and P. F. Jessen, 2003 : Swell transformation across the continental shelf. part I : Attenuation and directional broadening. *J. Phys. Oceanogr.*, **33**, 1921–1939.
- Ardhuin, F., N. Rasche, and K. A. Belibassakis, 2008b : Explicit wave-averaged primitive equations using a generalized Lagrangian mean. *Ocean Modelling*, **20**, 35–60.
- Ardhuin, F. and A. Roland, 2012 : Coastal wave reflection, directional spread, and seismoacoustic noise sources. *J. Geophys. Res.*, **117**, C00J20.

- 663 Ardhuin, F., N. Suzuki, J. McWilliams, and H. Aiki, 2017 : Comments on 'a combined
664 derivation of the integrated and vertically resolved, coupled wave-current equations'. *J.*
665 *Phys. Oceanogr.*, **47**, 2377–2385.
- 666 Ardhuin, F., et al., 2010 : Semi-empirical dissipation source functions for wind-wave models :
667 part I, definition, calibration and validation. *J. Phys. Oceanogr.*, **40**, 1917–1941.
- 668 Ardhuin, F., et al., 2012 : Numerical wave modeling in conditions with strong currents :
669 dissipation, refraction and relative wind. *J. Phys. Oceanogr.*, **42**, 2010–2112.
- 670 Bahaj, A. S. and L. E. Myers, 2004 : Analytical estimates of the energy yield potential from
671 the alderney race (channel islands) using marine energy converters. *Renewable Energy*, **29**,
672 1931–1945.
- 673 Bailly Du Bois, P. and F. Dumas, 2005 : Fast hydrodynamic model for medium- and long-
674 term dispersion in seawater in the english channel and southern north sea, qualitative and
675 quantitative validation by radionuclide tracers. *Ocean Modelling*, **9**, 169–210.
- 676 Bailly Du Bois, P., F. Dumas, L. Solier, and C. Voiseux, 2012 : In-situ database toolbox
677 for short-term dispersion model validation in macro-tidal seas, application for 2d-model.
678 *Continental Shelf Research*, **36**, 63–82.
- 679 Banihashemi, S., J. Kirby, and Z. Dong, 2017 : Approximation of wave action flux velocity
680 in strongly sheared mean flows. *Ocean Modelling*, **116**, 33–47.
- 681 Battjes, J. A. and J. P. F. M. Janssen, 1978 : Energy loss and set-up due to breaking of
682 random waves. *Proceedings of the 16th international conference on coastal engineering*,
683 ASCE, 569–587.
- 684 Bennis, A.-C., F. Ardhuin, and F. Dumas, 2011 : On the coupling of wave and three-
685 dimensional circulation models : Choice of theoretical framework, practical implementation
686 and adiabatic tests. *Ocean Modelling*, **40**, 260–272.
- 687 Bennis, A.-C., F. Ardhuin, T. Odaka, and F. Dumas, 2013 : Un nouveau modle coupl vagues-
688 courant 3D. *Paralia*, **6**, 8.1–8.12.
- 689 Bennis, A.-C., P. Bailly Du Bois, F. Dumas, C. Lathuillère, F. Adong, and J.-F. Filipot,
690 2018 : Towards a realistic numerical modelling of wave-current-turbulence interactions in
691 Alderney Race. *2018 OCEANS - MTS/IEEE Kobe Techno-Oceans (OTO)*, IEEE, 1–7.
- 692 Bennis, A.-C., F. Dumas, F. Ardhuin, and B. Blanke, 2014 : Mixing parameterization :
693 impacts on rip currents and wave set-up. *Ocean Engineering*, **42**, 213–227.

- 694 Bennis, A.-C., F. Dumas, and B. Blanke, 2016 : Modulation of wave-current interactions by
695 horizontal mixing and spatial resolution. *Ocean Modelling*, **99**, 75–85.
- 696 Boudiere, E., C. Maisondieu, F. Ardhuin, M. Accensi, L. Pineau-Guillou, and J. Lepesqueur,
697 2013 : A suitable metocean hindcast database for the design of marine energy converters.
698 *International Journal of Marine Energy*, **3**, 40–52.
- 699 Buis, S., A. Piacentini, and D. Déclat, 2008 : PALM : A computational framework for
700 assembling high performance computing applications. *Concurrency Computat. : Pract.*
701 *Exper.*, **18** (2), 247–262.
- 702 Burchard, H., 2001 : Simulating the wave-enhanced layer under breaking surface waves with
703 two-equation turbulence models. *J. Phys. Oceanogr.*, **31**, 3133–3145.
- 704 Christoffersen, J. B. and I. G. Jonsson, 1985 : Bed friction and dissipation in a combined
705 current and wave motion. *Ocean Eng.*, **12** (5), 387–423.
- 706 Coelingh, J., A. V. Wijk, and A. Holtslag, 1996 : Analysis of wind speed observations over
707 the North Sea. *Journal of Wind Engineering and Industrial Aerodynamics*, **61**, 51–69.
- 708 Coelingh, J., A. V. Wijk, and A. Holtslag, 1998 : Analysis of wind speed observations over
709 the North Sea. *Journal of Wind Engineering and Industrial Aerodynamics*, **73**, 125–144.
- 710 Coles, D. S., L. S. Blunden, and A. S., 2017 : Assessment of the energy extraction potential
711 at tidal sites around the channel islands. *Energy*, **124**, 171–186.
- 712 Craik, A. D. D. and S. Leibovich, 1976 : A rational model for Langmuir circulations. *J. Fluid*
713 *Mech.*, **73**, 401–426.
- 714 Dauvin, J.-C., 2015 : History of benthic research in the english channel : From general
715 patterns of communities to habitat mosaic description. *Journal of Sea Research*, **100**,
716 32–45.
- 717 Delpey, M., F. Ardhuin, P. Otheguy, and A. Jouon, 2014 : Effects of waves on coastal water
718 dispersion in a small estuarine bay. *J. Geophys. Res.*, **119**, 70–86.
- 719 Donelan, M. A., J. Hamilton, and W. H. Hui, 1985 : Directional spectra of wind-generated
720 waves. *Phil. Trans. Roy. Soc. London A*, **315**, 509–562.
- 721 Filipot, J.-F. and F. Ardhuin, 2012 : A unified spectral parameterization for wave breaking :
722 from the deep ocean to the surf zone. *J. Geophys. Res.*, **115**, C04022.

- 723 Foveau, A., S. Haquin, and J. Dauvin, 2017 : Using underwater imagery as a complementary
724 tool for benthos sampling in an area with high-energy hydrodynamic conditions. *Journal*
725 *of Marine Biology Oceanography*, **6**, 1–7.
- 726 Furgerot, L., P. Bailly Du Bois, Y. Méar, E. Poizot, and A.-C. Bennis, 2018 : Velocity profile
727 variability at a tidal-stream energy site (aldemey race, france) : From short (second) to
728 yearly time scales. *2018 OCEANS - MTS/IEEE Kobe Techno-Oceans (OTO)*, IEEE, 1–8.
- 729 Furgerot, L., Y. Poprawski, M. Violet, E. Poizot, P. Bailly Du Bois, M. Morillon, and
730 Y. Mear, 2019 : Mobile vs encrusted quaternary sediments and their bedrock in a tide-
731 dominated environment (Alderney Race). *Journal of Maps*, 1–19.
- 732 Grant, W. D. and O. S. Madsen, 1979 : Combined wave and current interaction with a rough
733 bottom. *J. Geophys. Res.*, **84**, 1797–1808.
- 734 Groeneweg, J. and G. Klopman, 1998 : Changes in the mean velocity profiles in the combined
735 wave-current motion described in GLM formulation. *J. Fluid Mech.*, **370**, 271–296.
- 736 Guillou, N., G. Chapalain, and S. P. Neill, 2016 : The influence of waves on the tidal kinetic
737 energy site. *Applied Energy*, **180**, 402–415.
- 738 Hashemi, M., S. Neill, P. Robins, A. Davies, and M. Lewis, 2015 : Effects of waves on the
739 tidal energy resource at a planned tidal stream array. *Renewable Energy*, **75**, 626–639.
- 740 Hasselmann, K., et al., 1973 : Measurements of wind-wave growth and swell decay during
741 the Joint North Sea Wave Project. *Deut. Hydrogr. Z.*, **8 (12)**, 1–95, suppl. A.
- 742 Hasselmann, S., K. Hasselmann, J. Allender, and T. Barnett, 1985 : Computation and pa-
743 rameterizations of the nonlinear energy transfer in a gravity-wave spectrum. Part II : Pa-
744 rameterizations of the nonlinear energy transfer for application in wave models. *J. Phys.*
745 *Oceanogr.*, **15**, 1378–1391, URL [http://ams.allenpress.com/archive/1520-0485/15/](http://ams.allenpress.com/archive/1520-0485/15/11/pdf/i1520-0485-15-11-1378.pdf)
746 [11/pdf/i1520-0485-15-11-1378.pdf](http://ams.allenpress.com/archive/1520-0485/15-11-1378.pdf).
- 747 Holmedal, L. E., D. Myrhaug, and H. Rue, 2000 : Seabed shear stresses under irregular
748 waves plus current from monte carlo simulations of parameterized models. *Coastal Eng.*,
749 **39**, 123–147.
- 750 Kantha, L. H. and C. A. Clayson, 2004 : On the effect of surface gravity waves on mixing in
751 the oceanic mixed layer. *Ocean Modelling*, **6**, 101–124.
- 752 Kemp, P. H. and R. R. Simons, 1982 : The interaction of waves and a turbulent current :
753 waves propagating with the current. *J. Fluid Mech.*, **116**, 227–250.

- 754 Kemp, P. H. and R. R. Simons, 1983 : The interaction of waves and a turbulent current :
755 waves propagating against the current. *J. Fluid Mech.*, **130**, 73–89.
- 756 Kumar, N., G. Voulgaris, J. C. Warner, and M. Olabarrieta, 2012 : Implementation of
757 the vortex force formalism in the coupled ocean-atmosphere-wave-sediment transport
758 (COAWST) modeling system for inner shelf and surf zone applications. *Ocean Model-*
759 *ling*, **47**, 65–95.
- 760 Larssonneur, C., P. Bouysse, and J.-P. Auffret, 1982 : The superficial sediments of the english
761 channel and its western approaches sedimentology. *Sedimentology*, 851–864.
- 762 Lazure, P. and F. Dumas, 2008 : An external-internal mode coupling for a 3d hydrodynamical
763 model for applications at regional scale (MARS). *Adv. Water Resources*, **31**, 233–250.
- 764 Leroy, R. and B. Simon, 2003 : Réalisation et validation d’un modèle de marée en Manche
765 et dans le golfe de Gascogne - Application à la réalisation d’un nouveau programme de
766 réduction de sondages bathymétriques.
- 767 Lewis, M., S. Neill, P. Robins, M. Hashemi, and S. Ward, 2017 : Characteristics of the
768 velocity profile at tidal-stream energy sites. *Renewable Energy*, 1–15.
- 769 Lewis, M. J., S. P. Neill, M. R. Hashemi, and M. Reza, 2014 : Realistic wave conditions and
770 their influence on the quantifying the tidal stream energy resource. *Applied Energy*, **136**,
771 495–508.
- 772 Lewis, M. J., S. P. Neill, P. E. Robins, and M. R. Hashemi, 2015 : Resource assessment for
773 future generations of tidal-stream energy arrays. *Energy*, **83**, 403–415.
- 774 Lopez, G., et al., 2018 : Hydrodynamics of the alderney race : HF radar wave measurements.
775 *Proceeding of the International Conference on Ocean Energy, France*, 1–6.
- 776 Lopez, G., et al., 2019 : Surface hydrodynamics of the alderney race from HF radar mea-
777 surements. *Proceeding of the 13th European Wave and Tidal Energy Conference, Italy*,
778 1–10.
- 779 Lynn, P. A., 2013 : *Electricity from Wave and Tide : An Introduction to Marine Energy*.
780 John Wiley and Sons Ltd, 276 pp.
- 781 Maisondieu, C., 2016 : Statistical characterization of complex sea-states in the bay of Biscay
782 for the design of marine structures. *Proceedings of the 15th Journées de l’Hydrohydyna-*
783 *mique, November 22–24, Brest, France*, 1–12.

- 784 Marechal, D., 2004 : A soil-based approach to rainfall-runoff modelling in un- gauged catch-
785 ments for england and wales. Ph.D. thesis, University of Cranfield, UK.
- 786 Mathisen, P. P. and O. S. Madsen, 1996a : Wave and currents over a fixed rippled bed.
787 2. bottom and apparent roughness experienced by currents in the presence of waves. *J.*
788 *Geophys. Res.*, **101 (C7)**, 16,543–16,550.
- 789 Mathisen, P. P. and O. S. Madsen, 1996b : Waves and currents over a fixed rippled bed.
790 1. bottom roughness experienced by waves in the presence and absence of currents. *J.*
791 *Geophys. Res.*, **101 (C7)**, 16,533–16,542.
- 792 Mathisen, P. P. and O. S. Madsen, 1999 : Wave and currents over a fixed rippled bed.
793 3. bottom and apparent roughness for spectral waves and currents. *J. Geophys. Res.*,
794 **104 (C8)**, 18,447–18,461.
- 795 McWilliams, J. C., J. M. Restrepo, and E. M. Lane, 2004 : An asymptotic theory for the
796 interaction of waves and currents in coastal waters. *J. Fluid Mech.*, **511**, 135–178.
- 797 Mellor, G., 2015 : A combined derivation of the integrated and vertically resolved, coupled
798 wave-current equations. *J. Phys. Oceanogr.*, **45**, 1453–1463.
- 799 Mellor, G., 2017 : Reply to comments on ‘a combined derivation of the integrated and
800 vertically resolved, coupled wave-current equations’. *J. Phys. Oceanogr.*, **47**, 2387–2389.
- 801 Mercier, P., 2019 : Modlisation de la turbulence engendre par la bathymtrie dans le raz
802 blanchard : Approche locale (lbm-les). Ph.D. thesis, Caen University, France.
- 803 Michaud, H., P. Marsaleix, C. Estournel, F. Bourrin, F. Lyard, C. Mayet, and F. Ardhuin,
804 2012 : Three-dimensional modelling of wave-induced current from the surf zone to the
805 inner shelf. *Ocean Science*, **8**, 657–681.
- 806 Moghimi, S., K. Klingbeil, U. Grawe, and H. Burchard, 2013 : A direct comparison of the
807 depth-dependent radiation stress method and a vortex force formulation within a three-
808 dimensional ocean model. *Ocean Modelling*, **70**, 132–144.
- 809 Nielsen, P., 1992 : *Coastal bottom boudary layers and sediment transport*. World Scientific
810 Publishing.
- 811 Okubo, A., 1971 : Oceanic diffusion diagram. *Deep Sea Research*, **18**, 789–802.
- 812 Phillips, O. M., 1958 : The equilibrium range in the spectrum of wind-generated waves. *J.*
813 *Fluid Mech.*, **4**, 426–433.

- 814 Shom, 2017 : Références altimétriques maritimes. URL [https://www.data.gouv.fr/fr/
815 datasets/references-altimetriques-maritimes/](https://www.data.gouv.fr/fr/datasets/references-altimetriques-maritimes/), ISBN 978-2-11-139469-8.
- 816 Signell, R. P., R. C. Beardsley, H. C. Graber, and C. Capotondi, 1990 : Effect of wave-current
817 interaction on wind-driven circulation in narrow, shallow embayments. *J. Geophys. Res.*,
818 **95 (C6)**, 9671–9678.
- 819 Sleath, J. F. A., 1991 : Velocities and shear stresses in wave-current flows. *J. Geophys. Res.*,
820 **96 (C8)**, 15 237–15 244.
- 821 Smagorinsky, J., 1963 : General circulations experiments with the primitive equations i. the
822 basic experiment. *Monthly Weather Review*, **8**, 99–165.
- 823 Soulsby, R. L., 1995 : Bed shear stresses due to combined waves and currents. In : Stive,
824 M., Fredsøe, J., Hamm, L., Soulsby, R., Teisson, C., Winterwerp, J. (Eds). *Advances in
825 Coastal Morphodynamics, Delft Hydraulics, Delft, The Netherlands*, 420–423.
- 826 Soulsby, R. L., L. Hamm, G. Klopman, D. Myrhaug, R. R. Simons, and G. P. Thomas, 1993 :
827 Wave-current interaction within and outside the bottom boundary layer. *Coastal Eng.*, **21**,
828 41–69.
- 829 Thiebault, M. and A. Sentchev, 2017 : Asymmetry of tidal currents off W. Brittany coast
830 and assessment of tidal energy resource around ushant island. *Renewable Energy*, **105**,
831 735–747.
- 832 Thiebault, M., A. Sentchev, and P. Bailly-Du-Bois, 2019 : Merging velocity measurements
833 and modeling to improve understanding of tidal stream resource in alderney race. *Energy*,
834 **178**, 460–470.
- 835 Thiebot, J., P. B. du Bois, and S. Guillou, 2015 : Numerical modeling of the effect of tidal
836 stream turbines on the hydrodynamics and the sediment transport : Application to the
837 Alderney Race (Raz Blanchard), France. *Renewable Energy*, **75**, 356 – 365.
- 838 Toba, Y., 1973 : Local balance in the air-sea boundary processes. II partition of wind stress
839 to waves and current. *J. Oceanogr. Soc. Japan*, **29**, 70–75, URL [http://www.terrapub.
840 co.jp/journals/J0/JOSJ/pdf/2902/29020070.pdf](http://www.terrapub.co.jp/journals/J0/JOSJ/pdf/2902/29020070.pdf).
- 841 Togneri, M., M. Lewis, S. Neill, and I. Masters, 2017 : Comparison of ADCP measurements
842 and 3D model simulations of turbulence at a tidal energy site. *Renewable Energy*, 1–10.
- 843 Tolman, H. L. and al., 2014 : User manual and system documentation of WAVEWATCH-
844 IIITM version 4.18. Tech. Rep. 282, NOAA/NWS/NCEP/MMAB.

- 845 Uchiyama, Y., J. C. McWilliams, and J. M. Restrepo, 2009 : Wave-current interaction in
846 nearshore shear instability analyzed with a vortex force formalism. *J. Geophys. Res.*, **114**.
- 847 Uchiyama, Y., J. C. McWilliams, and A. F. Shchepetkin, 2010 : Wave-current interaction
848 in oceanic circulation model with a vortex-force formalism Application to the surf zone.
849 *Ocean Modelling*, **34**, 16–35.
- 850 Valcke, S., T. Craig, and L. Coquart, 2015 : OASIS3-MCT User Guide. Tech. rep., CERFACS.
- 851 Walstra, D. J. R., J. Roelvink, and J. Groeneweg, 2000 : Calculation of wave-driven currents
852 in a 3D mean flow model. *Proceedings of the 27th International Conference on Coastal*
853 *Engineering, Sydney*, ASCE, Vol. 2, 1050–1063.
- 854 Warner, J., B. Armstrong, R. He, and J. Zambon, 2010 : Development of a coupled ocean-
855 atmosphere-wave-sediment transport (COAWST) modeling system. *Ocean Modelling*, **35**,
856 230–244.
- 857 Warner, J. C., C. R. Sherwood, H. G. Arengo, and R. P. Signell, 2005 : Performance of four
858 turbulence models implemented using a generic length scale method. *Ocean Modelling*, **8**,
859 81–113.
- 860 Wolf, J. and D. Prandle, 1999 : Some observations of wave–current interaction. *Coastal Eng.*,
861 **37**, 471–485.
- 862 Xie, L., K. Wu, L. Pietrafesa, and C. Zhang, 2001 : A numerical study of wave-current
863 interactions through surface and bottom stresses : wind-driven circulation in the South
864 Atlantic Bight under uniform winds. *J. Geophys. Res.*, **106 (C8)**, 16 841–16 855.
- 865 Zhang, H., O. S. Madsen, S. A. Sannasiry, and E. S. Chan, 2004 : Hydrodynamic model
866 with wave-current interaction in coastal regions. *Estuarine, Coastal and Shelf Science*, **61**,
867 317–324.
- 868 Zieger, S., A. V. Babanin, W. E. Rogers, and I. R. Young, 2015 : Observation- based source
869 terms in the third-generation wave model wavewatch. *Ocean Modelling*, **96**, 2–25.